Check for updates

Recent advances in bifunctional carbon-based single-atom electrocatalysts for rechargeable zinc–air batteries

Yang Chen,[a,b] Gan Wang,[b] Junhua Li,[a] Ting He, [ID][d] Yi Zhang, [ID] *[a,b]
Heng Zhang [ID] *[c] and You-Nian Liu [ID] *[a,b]

Rechargeable zinc–air batteries (R-ZABs) have substantial potential for future large-scale applications owing to their sustainability, intrinsic safety, and high energy density. However, R-ZABs still lag behind the remarkable success of lithium-ion batteries (LIBs) to date. A crucial factor in advancing sustainable R-ZABs is the development of efficient bifunctional oxygen electrocatalysts, since they are currently constrained by the slow kinetics of the oxygen reduction reaction (ORR) and the oxygen evolution reaction (OER) at the air electrodes. Recently, carbon-based single-atom catalysts (C-SACs) have emerged as leading candidates among available oxygen electrocatalysts due to their high atom efficiency, adaptable structures, and outstanding catalytic activity. The growing interest in bifunctional C-SACs necessitates a thorough exploration of their reaction mechanisms and strategies for design and modification toward effective enhancement of ORR and OER performance. In this review, we begin by outlining the fundamental composition and reaction mechanisms of R-ZABs. We then delve into six atomic-scale modulation strategies of C-SACs in detail, emphasizing the relationship between structure and performance to aid in the development of highly efficient bifunctional electrocatalysts. The fundamental insights into the dynamic structural changes and the mechanisms of ORR/OER for C-SACs are presented by integrating *in situ* and/or *operando* characterizations with theoretical calculations. We also provide an overview of the latest advancements in C-SACs for sustainable R-ZABs, focusing on different types of carbon precursor and the impact of carbon nanostructures on electrocatalytic performance. Finally, we discuss future perspectives and challenges associated with C-SACs in R-ZABs. This review aims to offer practical and inspiring guidance for the exploration of optimal C-SACs and further enhancement of sustainable R-ZAB performance.

1. Introduction

To address the excessive consumption of fossil fuels and the increasingly serious environmental problems, it is imperative to advance renewable and efficient energy conversion technologies.[1–3] Emerging energy storage and conversion devices, such as fuel cells, metal-ion batteries, and metal–sulfur batteries, present promising avenues for harnessing sustainable electricity.[4–9] Among them, lithium-ion batteries (LIBs) have become integral to our daily life after decades of

[a]Key Laboratory of Functional Metal–Organic Compounds of Hunan Province, College of Chemistry and Materials Science, Hengyang Normal University, Hengyang 421008, China. E-mail: yzhangcsu@csu.edu.cn, liuyounian@csu.edu.cn
[b]College of Chemistry and Chemical Engineering, Central South University, Changsha 410083, China
[c]Institute for Materials Science and Devices, School of Materials Science & Engineering, Suzhou University of Science and Technology, Suzhou 215009, China. E-mail: zhangheng@usts.edu.cn
[d]School of Materials Science and Engineering, Xiangtan University, Xiangtan, Hunan 411105, China

development. Despite their commercial success, LIBs face challenges including the limited energy density, low abundance of lithium (Li) resources, and potential safety issues.[10,11] To counter these issues, aqueous metal–air batteries (metal: zinc, iron, aluminum, magnesium and lithium) have garnered significant interest in recent years.[8,12,13] Among them, the zinc anode is particularly suitable for use with aqueous electrolytes due to its excellent corrosion resistance in alkaline solutions and high reversibility.[13,14] Zinc–air batteries (ZABs) boast a nearly 140-year history since their inception in 1878, during which they have adapted to meet rapidly changing technological needs.[15] Notably, ZABs can be combined with various energy sources to leverage synergistic benefits. For example, a number of ZAB systems have incorporated light-assisted strategies to enhance their output efficiency.[16] Currently, zinc metal is considerably cheaper than Li metal ($2.6 *vs.* $20 per kg), and ZABs offer a theoretical energy density (1350 W h kg^{-1}) more than three times that of LIBs.[17–20] Additionally, the advantages of non-pollution, sustainability, being hazard-free, and the low technological

requirements of ZABs have also established a solid foundation for their green commercial application.[8,21,22] The technology for primary ZABs (P-ZABs) was advanced, finding applications in devices such as hearing aids, railway signals, and various other equipment. These batteries demonstrated impressive specific and volumetric energy densities, reaching up to 442 W h kg^{-1} and 1672 W h L^{-1}, respectively, in button cell configurations.[23] As we transition into an era focused on sustainable development, ZABs, one of the oldest forms of energy storage, are increasingly recognized globally as a promising area of research and a viable solution for building a sustainable future.[15]

The P-ZABs, despite their commercialization, face significant challenges, including resource waste and practical usage issues, which highlights the pressing necessity for the development of rechargeable ZABs (R-ZABs). However, the transition from P-ZABs to R-ZABs has been hindered by the morphological alterations of the zinc anode, the slow kinetics associated with the oxygen reduction/evolution reaction (ORR/OER) at the cathode and electrolyte stability issues.[24,25] The first two are particularly formidable challenges. Although researchers have made significant strides in resolving numerous persistent issues associated with zinc electrodes, such as shape distortion and maximizing zinc utilization at high charging rates, R-ZABs still face challenges with high polarization of the ORR/OER at the air cathode.[14,26,27] Typically, the round-trip energy efficiencies of R-ZABs fall below 55–65%.[20] Therefore, lowering the overpotential of the ORR/OER by employing highly efficient bifunctional electrocatalysts is crucial for improving the performance and feasibility of R-ZABs, paving the way for their practical applications. Currently, the physical mixture of Pt/C and IrO$_2$/RuO$_2$ is generally regarded as the benchmark bifunctional catalyst, but its high cost and inferior stability are obstacles to the requirements for large-scale commercialization for R-ZABs.[28–31]

The advancements of ORR/OER catalysts for R-ZABs began in 2012, when Chen *et al.* synthesized a novel core–corona-structured bifunctional oxygen electrocatalyst, featuring LaNiO$_3$ centers supported by nitrogen-doped carbon nanotubes.[43] In the past, various types of transition metal-based bifunctional oxygen catalysts, such as metal oxides, metal sulfides, alloys, and single-atom catalysts (SACs), have been extensively explored as cost-effective alternatives to noble metal materials to enhance the performance of R-ZABs.[44–47] In particular, SACs have garnered significant interest compared with conventional nanoparticles or bulk catalysts, owing to their nearly 100% atomic utilization, unsaturated coordination centers, and unique quantum size effects (Fig. 1).[48–51] However, SACs tend to agglomerate during synthesis due to their high surface energy. To address this issue, various substrates have been utilized to stabilize isolated single atoms. Metal oxides and hydroxides, characterized by abundant defect sites and –OH groups, serve as ideal supports for SACs and demonstrate remarkable performance.[52–54] Monolayer 2D transition metal dichalcogenides are known for their excellent electrical conductivity and large specific surface area, making them suitable substrates for hosting SACs and studying their electrochemical properties.[55,56] Additionally, metal element substrates can anchor other metal atoms, resulting in unique single-atom metal alloys with enhanced electrocatalytic properties due to strong metal interactions.[57,58] Moreover, available supports for SACs also include metal nitrides, carbides, phosphides, and metal–organic frameworks (MOFs).[59–61] Especially, carbon materials feature flexible internal heteroatoms (like N, P, S) and strong interactions with metals, providing spatial confinement that helps prevent agglomeration and alters the electronic and geometric structures as well as the charge density of the metal atoms.[62–64] Furthermore, the high surface area, excellent conductivity, and hierarchical pore structure of carbon materials are crucial for efficient mass and electron transfer, enhancing accessibility between reactants and active sites—advantages that pure metal oxides, hydroxides, or perovskites lack.[60,65] Additionally, the structural diversity and design flexibility of carbon materials (such as amorphous carbon, graphite, and diamond) allow for the investigation of precise structure–performance relationships, which are vital for a deeper understanding of catalytic mechanisms and the development of high-performance catalysts.

Against this backdrop, carbon-based single-atom catalysts (C-SACs) have been explored and successfully employed as

Yang Chen is currently a lecturer at the College of Chemistry and Materials Science, Hengyang Normal University, China. He received his B.S. degree and Ph.D. degree from Central South University in 2018 and 2023, respectively. His current research focuses on the synthesis of single-atom-based electrocatalysts for application in rechargeable zinc–air batteries.

Yang Chen

Gan Wang is currently a Ph.D. student at the Central South University. He received his M.S. degree from the College of Chemistry and Chemical Engineering, Xinjiang University. His current research interests focus on energy photocatalysis/electrocatalysis and zinc–air batteries.
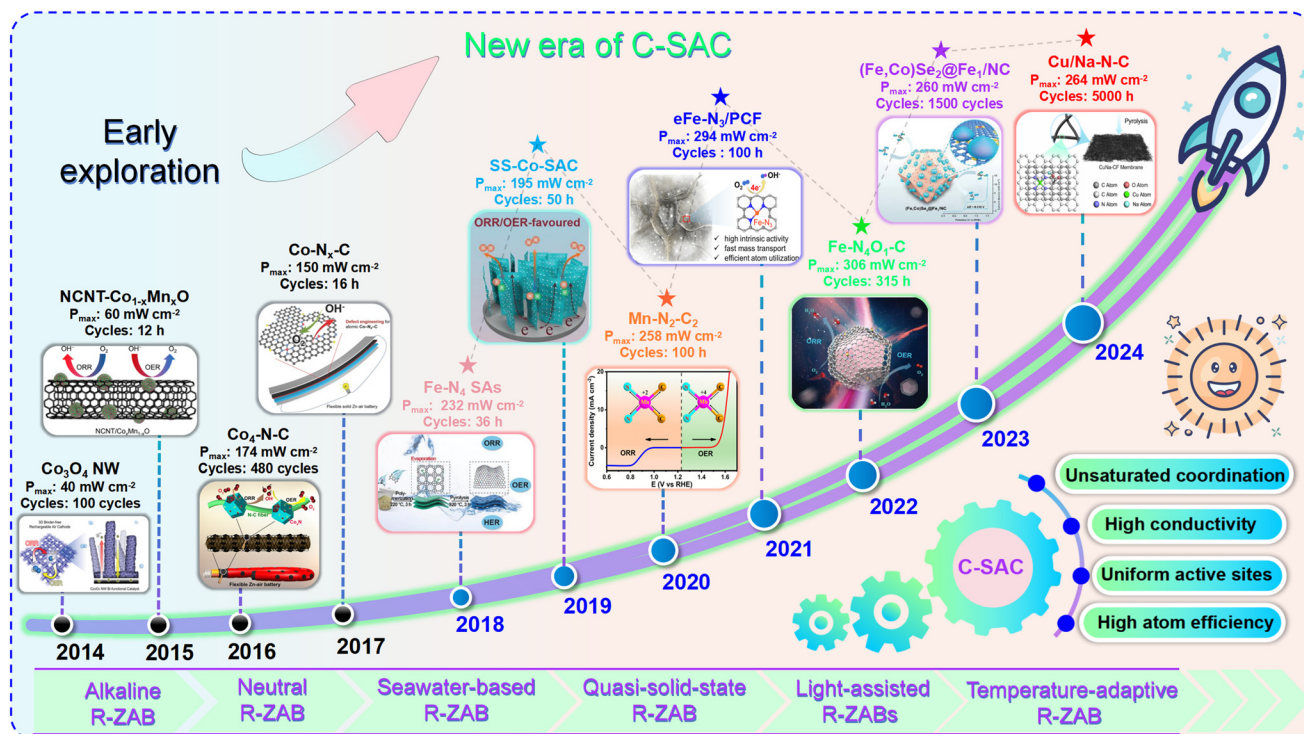
Gan Wang

This journal is © The Royal Society of Chemistry 2025

Fig. 1 Timeline of outstanding representative works on bifunctional C-SACs for R-ZABs. The image of Co_3O_4 NW. Reproduced with permission.[32] Copyright 2014, Wiley-VCH. The image of NCNT-$Co_{1-x}Mn_xO$. Reproduced with permission.[33] Copyright 2015, Elsevier B. V. The image of Co_4−N−C. Reproduced with permission.[34] Copyright 2016, American Chemical Society. The image of Co−N_x−C. Reproduced with permission.[35] Copyright 2017, Wiley-VCH. The image of Fe−N_4 SAs. Reproduced with permission.[36] Copyright 2018, Wiley-VCH. The image of SS-Co-SAC. Reproduced with permission.[37] Copyright 2019, Wiley-VCH. The image of Mn−N_2−C_2. Reproduced with permission.[38] Copyright 2020, American Chemical Society. The image of eFeN$_3$-PCF. Reproduced with permission.[39] Copyright 2021, Elsevier B. V. The image of Fe−N_4O_1−C. Reproduced with permission.[40] Copyright 2022, Wiley-VCH. The image of (Fe, Co)Se$_2$@Fe$_1$/NC. Reproduced with permission.[41] Copyright 2023, Wiley-VCH. The image of Cu/Na−N−C. Reproduced with permission.[42] Copyright 2024, Springer Nature.

heterogeneous catalysts for oxygen electrocatalytic process.[66–69] However, as the demand for catalytic performance increases, C-SACs are facing several urgent issues. (1) The active sites with symmetrical electronic structure may not achieve the optimal adsorption of intermediates; (2) balancing activity and stability remains challenging; (3) a trade-off between ORR and OER performance due to the volcano relationship may occur; (4) the carbon-based substrates would be electro-oxidized to

Ting He obtained her Ph.D. degree in chemistry at Central South University under the supervision of Prof. Yi Zhang and Juan Xiang. She is currently affiliated with the School of Materials Science and Engineering, Xiangtan University. Her research interests include the design and synthesis of metal single-atom catalysts and their application in energy storage and conversion.

Ting He

Yi Zhang obtained his Ph.D. degree from the Institute of Chemistry, Chinese Academy of Science (ICCAS), as a coeducated Ph.D. candidate between the ICCAS and the Max Planck Institute of Colloids and Interfaces. He is currently a full professor at Central South University, Changsha, China. His research interests include supramolecular hydrogels and aerogels, transition-metal-based sub-nanocatalysts for electrochemical reduction of CO_2, O_2, and energy conversion.

Yi Zhang

CO_2 under high electrical potentials, which would result in carbon surface destruction and ruin active catalytic sites. Fortunately, the tunable coordination structures and electronic environments of C-SACs offer promising pathways to overcome limitations and further enhance the catalytic capacity. For instance, altering the charge and electron spin state of the active center through a heteroatoms doping strategy is effective in enhancing their catalytic activity.[70–73]

In recent years, we have witnessed the flourishing development of C-SACs in the fields of bifunctional oxygen catalysis (Fig. 1). Although previous reviews have effectively summarized the novel progress in bifunctional electrocatalysts for ZABs, there remains a need for more comprehensive and up-to-date reviews, particularly those focusing on C-SACs. This review begins with a concise overview of the components and operational principles of overall R-ZABs, followed by an in-depth examination of various electronic regulation strategies employed in C-SACs, alongside their structure–property relationship at the atomic level. We have also placed strong emphasis the study of the dynamic structural evolution and reaction mechanisms of C-SACs during ORR/OER using *in situ* and/or *operando* characterizations. The review also systematically summarizes recent advances in SACs anchored on various carbon substrates, including conventional carbon, MOF-derived carbon, biomass-derived carbon and small-molecule and polymer-derived carbon for bifunctional ORR/OER in R-ZABs (Fig. 2). Key cases are highlighted to illustrate how catalyst structure impacts R-ZAB performance. Finally, the review outlines the challenges and future prospects of bifunctional C-SACs in R-ZAB applications.
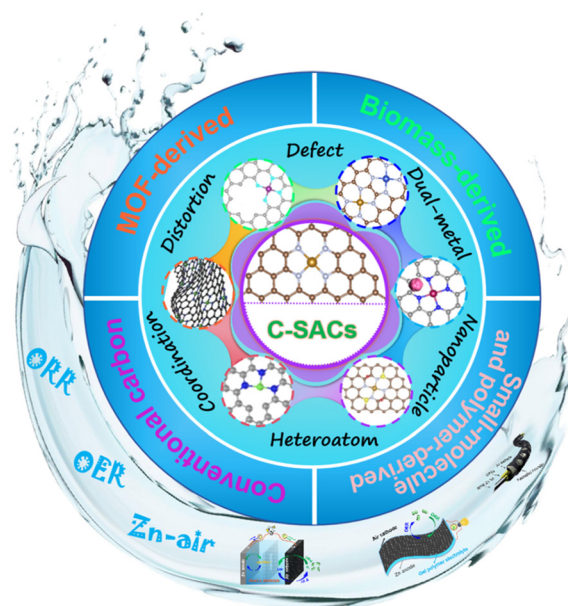
2. Fundamentals of zinc–air batteries

2.1. Battery components and working principles

As complex electrochemical systems, the components of two types of ZABs, namely aqueous ZABs and quasisolid-state

Fig. 2 Atomic-level regulation strategies and classification of bifunctional C-SACs for R-ZABs.

ZABs, are similar, and contain zinc anode, separator, alkaline electrolyte as well as air cathode (Fig. 3a and b). Usually, fresh Zn plates or Zn foils are used as the anode to guarantee sufficient discharge capacities. The general aqueous electrolyte consisting of 6 M KOH and $Zn(Ac)_2$ or $ZnCl_2$ additive can ensure maximum ionic conductivity and the reversibility of the Zn anode, thus in turn improving the overall performance of ZABs. Furthermore, gel polymers featuring 3D network structures are frequently employed to construct flexible ZABs in order to accommodate the demands of portable electronic devices and wearable technology. These polymers can effectively retain alkaline solutions while facilitating unobstructed ion diffusion pathways. In this situation, a separator is unnecessary if the anode and cathode can be stably riveted. At

Heng Zhang is currently a lecturer at the College of Materials Science and Engineering, Suzhou University of Science and Technology. He received his M.S. degree from Xinjiang University in 2019. He received his Ph.D. degree from Southwest University in 2022. His current research interests focus on energy and environmental materials for Na-ion, RT-Na/S batteries.

Heng Zhang

You-Nian Liu is currently a professor at the College of Chemistry and Chemical Engineering, Central South University, Hunan, China. He is also a council member of the Chemical Industry and Engineering Society of China. He obtained his Ph.D. degree from Central South University in 2002. His current research interests focus on the design and application of energy catalytic materials and the development of catalytic nanomaterials for immunomodulation.
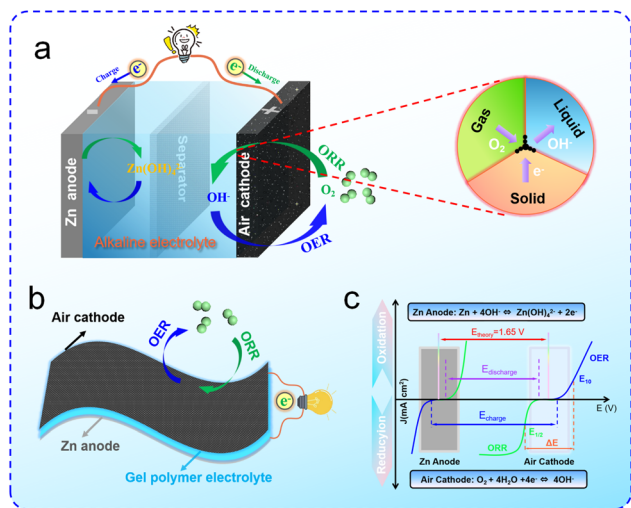
You-Nian Liu

Fig. 3 Illustration of two structures of R-ZABs: (a) liquid type and (b) quasi-solid-state type. (c) Polarization curves for Zn anode and air cathode for R-ZABs, revealing origin of theoretical discharge/charge potential of R-ZABs.
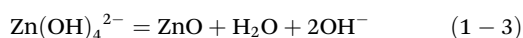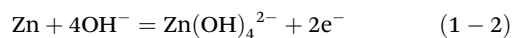
present, there has been significant research into hydrogels such as polyvinyl alcohol (PVA), polyacrylic acid (PAA), polyacrylamide (PAM), and sodium polyacrylate (PANa).[74] The air cathode is orderly composed of a catalytic layer, current collector (*e.g.* nickel foam and carbon paper) and gas diffusion layer.

In R-ZAB systems, electricity can be reversibly released and stored *via* the cathodic ORR/OER and anodic Zn dissolution/deposition processes (Fig. 3c). However, due to the polarization behavior of the ZAB during operation, its actual output voltage is often lower than the theoretical voltage value (1.65 V). When a ZAB discharges under alkaline conditions, O_2 from the air diffuses into the surface of the catalysts and is then reduced to OH^- ions. Simultaneously, Zn^{2+} ions produced by Zn anode oxidation will combine with the migrated OH^- ions to yield soluble $Zn(OH)_4^{2-}$ ion, which can further convert to insoluble ZnO if its concentration is saturated. Unfortunately, insulated ZnO may damage the initial electrolyte|Zn interfaces and hinder reactions on the Zn anode, thus ultimately lowering the overall efficiency of the battery. The discharge reaction is as follows:
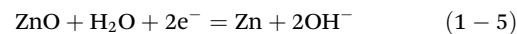
Air cathode:

$$O_2 + 2H_2O + 4e^- = 4OH^- \quad (1-1)$$

Zn anode:

$$Zn + 4OH^- = Zn(OH)_4^{2-} + 2e^- \quad (1-2)$$

$$Zn(OH)_4^{2-} = ZnO + H_2O + 2OH^- \quad (1-3)$$
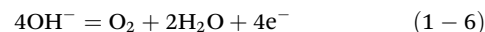
Overall reaction:

$$2Zn + O_2 = 2ZnO \quad (1-4)$$

During the charging process of R-ZABs, all involved reactions are completely the reverse process of the discharge reac-

tion, including that the Zn^{2+} ions in the electrolyte are reduced to metallic Zn and deposited on the anode surface and OH^- ions are oxidized to O_2 at the cathode. The charge reaction is as follows:

Zn anode:

$$ZnO + H_2O + 2e^- = Zn + 2OH^- \quad (1-5)$$

Air cathode:

$$4OH^- = O_2 + 2H_2O + 4e^- \quad (1-6)$$

Overall reaction:

$$2ZnO = 2Zn + O_2 \quad (1-7)$$

There are only simple solid–liquid reactions between Zn anode and alkaline electrolytes. However, the air cathode encounters a relatively complex tri-phase boundary reaction, which needs further follow-up with interest (Fig. 3a). The above analysis indicated that bifunctional electrocatalysts play an important role in the reversible transformation of OH^-/O_2 in the air cathode. Exploiting high-performance ORR/OER electrocatalysts is a research highlight in R-ZABs. The recent developments in oxygen electrocatalysts will be thoroughly discussed in the next section.

2.2. Battery performance evaluation

In ZAB systems, some significant evaluation parameters are required for qualitative assessment of the performance of bifunctional oxygen electrocatalysts and ZABs. Accordingly, we recommend some relevant definitions of basic parameters for better understanding. Half-potential ($E_{1/2}$) for the ORR: the potential to reach half of the ORR limiting current density. Potential at 10 mA cm^{-2} (E_{10}) for the OER: the potential to reach an OER current density of 10 mA cm^{-2}. The potential gap (ΔE) for ORR/OER: the difference between E_{10} and $E_{1/2}$. Typically, a smaller ΔE value indicates better bifunctional catalytic activity. Tafel slope: the linear relationship between overpotential and current density logarithm, which is a key parameter for appraising the kinetic rate. Power density for ZABs: the product of current density and voltage during ZAB discharge, the maximum value (P_{max}) of which is used for evaluating battery performance. Open-circuit voltage (OCV): the voltage difference between the cathode and anode when there is no current. Cycle life: the number of operating cycles or time which ZABs can achieve during continuous charging and discharging processes. The charging–discharging gap (ΔE): the difference between charging voltage and discharging voltage. Specific capacity: the quantity of electricity released by a unit mass of Zn anode. Energy density: the amount of energy stored in a certain space or active material.

2.3. Alkaline/neutral R-ZABs

An ideal R-ZAB electrolyte typically possesses several key properties: (i) high solubility and swift diffusion of O_2, (ii) a broad electrochemical window, (iii) low volatility and security, and (iv) a stable interface between the electrolyte and electrode.[14]

Based on the electrolyte's pH, R-ZABs can primarily be classified into two categories: alkaline and neutral ZABs. In general, the alkaline electrolytes are highly concentrated KOH, NaOH, or LiOH solutions with soluble Zn salts. Among them, KOH is often favored due to its excellent ionic conductivity, quick electrochemical kinetics, and moderate viscosity.[14] Importantly, in contrast to traditional ZABs utilizing freshwater electrolytes, recent advancements have led to the successful development of alkaline seawater-based ZABs (Fig. 4a).[75,76] Zhang's group was the first to create seawater-based ZABs, demonstrating that their performance in terms of polarization, capacity, and rate was on par with freshwater-based R-ZABs (Fig. 4b and c).[77] However, the complex ions in seawater, especially chloride ions, may block the active sites of the electrocatalysts and hinder the ORR/OER kinetics via mul-

tiple mechanisms.[78–80] Consequently, there is an urgent demand for durable bifunctional electrocatalysts that are highly resistant to chlorides to accelerate the development of seawater-based R-ZABs.

Typically, alkaline R-ZABs outperform neutral R-ZABs due to their strong O_2 redox capacity and enhanced ionic conductivity.[14] However, the alkaline electrolytes may react with atmospheric CO_2, leading to the production of insoluble carbonate byproducts and causing irreversible electrolyte degradation (Fig. 4c).[81] In contrast, neutral electrolytes, which are environmentally friendly, are largely unaffected by CO_2, maintaining electrolyte stability and the reversibility of the Zn anode. Currently, NH_4Cl solution, KNO_3 solution, PBS buffer solution, and soluble Zn salt-based electrolytes are commonly employed in the construction of neutral R-ZABs.[82,83] Nevertheless,
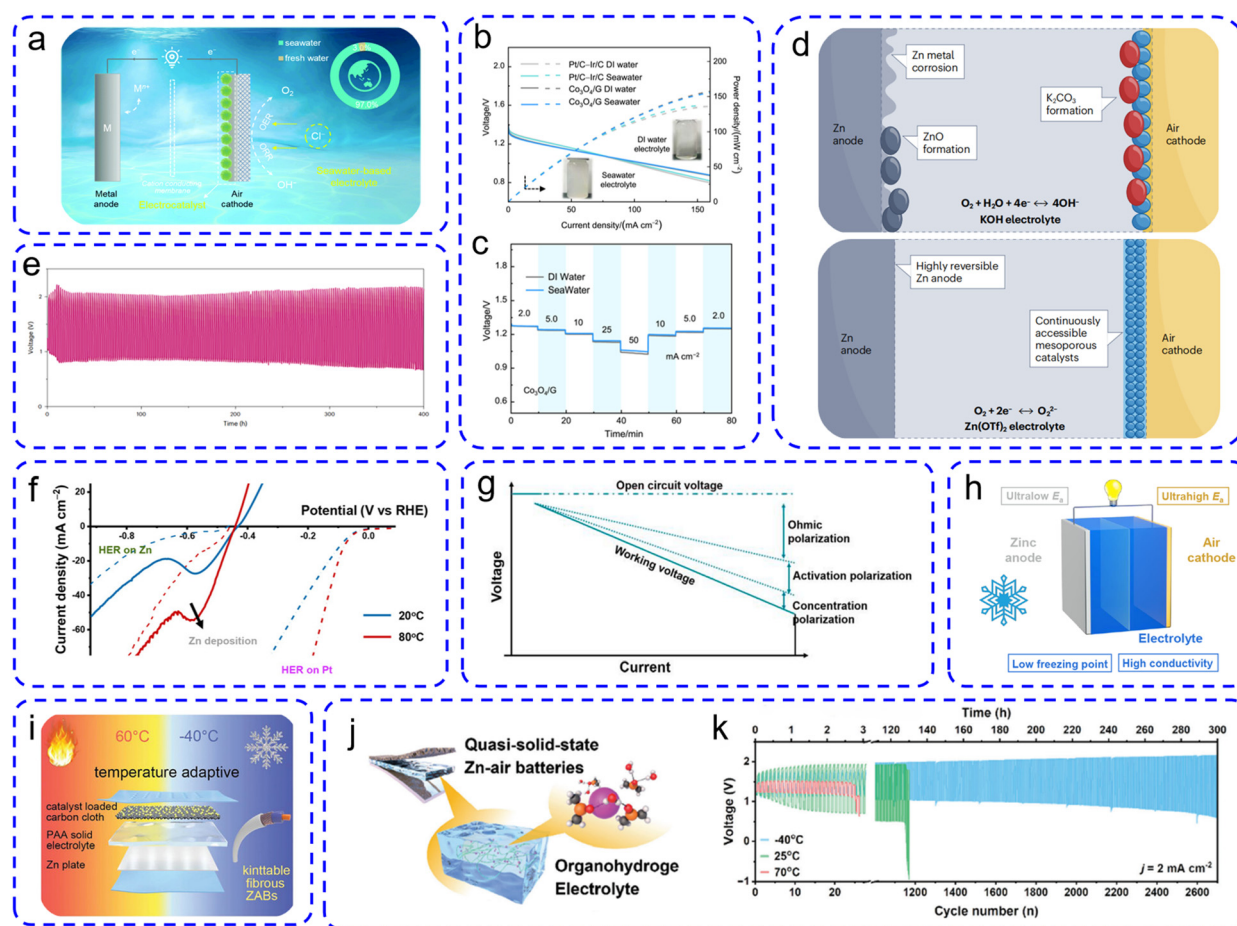

Fig. 4 (a) A schematic illustration of the basic structure and mechanism of a seawater-based metal–air battery. Reproduced with permission.[76] Copyright 2020, The Royal Society of Chemistry. (b) Power density curves and (c) discharge rate performances of the ZABs with different electrocatalysts using DI water-based and natural seawater-based electrolytes. Reproduced with permission.[77] Copyright 2020, Elsevier B.V. (d) Schematic of conventional alkaline (top) and neutral (bottom) ZABs chemistry. Reproduced with permission.[81] Copyright 2024, Springer Nature. (e) Long-term cycling performance of neutral ZABs. Reproduced with permission.[12] Copyright 2024, Springer Nature. (f) LSV curves of zinc deposition on zinc electrodes and HER on zinc electrodes. Reproduced with permission.[85] Copyright 2022, Wiley-VCH. (g) Schematic diagram of battery polarization. Reproduced with permission.[86] Copyright 2021, Elsevier B.V. (h) Schematic diagram of the inherent advantages of ZABs for low-temperature energy storage. Reproduced with permission.[87] Copyright 2021, Wiley-VCH. (i) Schematic illustration of the structure of temperature-adaptive solid-state ZAB. Reproduced with permission.[88] Copyright 2023, Wiley-VCH. (j) The quasi-solid ZABs system analysis. (k) Charging/discharging performance of R-ZABs at −40, 25, and 70 °C. Reproduced with permission.[89] Copyright 2023, Wiley-VCH.

the discharge products and reaction mechanisms of neutral R-ZABs vary significantly and are heavily influenced by the type of electrolyte used. For example, Xie *et al.* developed R-ZABs utilizing a neutral electrolyte composed of 4.0 M NH_4Cl and 2.0 M KCl, which exhibited a high P_{max} of 90.4 mW cm^{-2}, and superior rechargeable stability (>100 h) with a small ΔE of 1.19 V.[84] Zhang and co-workers reported a highly reversible $2e^-/O_2$ process with Zn/ZnO_2 chemistry in neutral electrolytes. The resulting neutral R-ZAB showed unprecedentedly stable performances (~400 h) with energy efficiencies of 61% (Fig. 4e).[12] The innovation and progress in neutral R-ZAB design offer a promising and sustainable approach for future energy storage technologies.

2.4. Temperature-adaptive R-ZABs

The feasibility of R-ZABs operating at full temperature has been a persistent issue for researchers. The highly concentrated alkaline aqueous electrolyte (6 M KOH + 0.2 M Zn $(OAc)_2$) demonstrates a higher boiling point (115 °C) and a lower freezing point (−44 °C) compared with pure water according to the colligative properties of solution, which could be beneficial for developing full-temperature adaptive R-ZABs.[85,87] In extreme operational conditions, the entropy of the electrochemical reactions is significantly influenced by temperature. Zhang's group systematically studied the chemical behavior of R-ZABs at sub-zero/high temperatures, demonstrating the enormous potential of R-ZABs for wide-temperature electrochemical energy storage.[85,87] High temperature induced the increased ion conductivity, the favored cathode kinetics, and the anti-passivation inherency of the Zn anode, all of which could minimize internal resistance and boost the performance of R-ZABs. However, the kinetics of the parasitic hydrogen evolution reaction (HER) on the Zn anode are obviously accelerated, resulting in the deterioration of the anode Faraday efficiency (FE) during charging and the reduction of battery cycling durability (Fig. 4f).[85] Notably, unfavored anode FE and electrolyte volatilization are severe yet not deadly to R-ZABs, which have been demonstrated to stably cycle at temperatures reaching 80 °C or even higher.

At low-temperature conditions, R-ZABs typically experience a reduced output voltage and limited power density due to significant activation, ohmic, and concentration polarization (Fig. 4g).[86] However, the ultrahigh and ultralow activation energies of the cathode and anode reactions in R-ZABs, respectively, mean that there is little impact on electrode kinetics at lower temperatures (Fig. 4h).[87] The primary constraint on the performance of low-temperature R-ZABs is the ohmic polarization caused by low electrolyte conductivity. To enhance the performance of R-ZABs in extreme conditions, various electrolyte modification strategies have been employed.[74,90,91] Alkaline hydrogel electrolytes are commonly utilized to develop temperature-adaptive R-ZABs.[74,92,93] These polymeric hydrogels contain numerous hydrophilic functional groups (such as –OH, –COOH, –NH_2, –SO_3) that can establish hydrogen bonds with free water molecules. The microporous structure within the hydrogels, along with the hydrogen bonding,
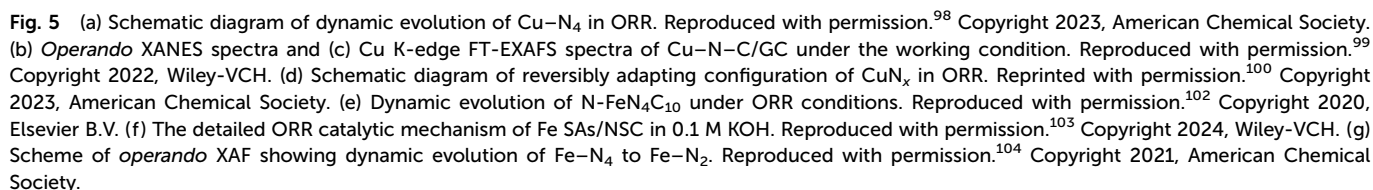
helps retain more H_2O molecules, thereby mitigating freezing and drying issues (Fig. 4i).[88] Furthermore, the inclusion of organic solvents like dimethyl sulfoxide (DMSO), ethylene glycol (EG), and glycerol enhances the environmental resilience of R-ZABs.[14,94] For instance, DMSO not only forms hydrogen bonds with water molecules to prevent ice crystal formation but also partially substitutes for water in the solvated structure of Zn^{2+}, which helps suppress the growth of Zn dendrites and reduces the activity of the HER.[95] Wei *et al.* developed quasi-solid R-ZABs using PAM-DMSO organic hydrogel as the electrolyte, which demonstrated impressive long-term cycling stability across a broad temperature range, attributed to their exceptional water retention capabilities (Fig. 4j and k).[89]

3. Dynamic structure evolution of C-SACs

ORR/OER encompasses a variety of processes, such as the diffusion, adsorption and desorption of reactant species, as well as multi-electron transfer within electrocatalysts.[55] Unlike the traditional view of catalysts in physical chemistry, recent findings indicate that most catalysts undergo structural changes during chemical reactions.[96] Therefore, it is crucial to examine the structural evolution of C-SACs to pinpoint the real catalytic active sites, which is vital for understanding the relationship between catalyst structure and catalytic activity. Additionally, a deep knowledge of the dynamic reaction mechanisms can enhance the design of the optimal electronic structure of C-SACs, which is closely tied to the adsorption characteristics of reactants and their intermediates. Fortunately, the recent advancements in *in situ* and *operando* characterization techniques have made it possible to monitor dynamic catalytic behavior and uncover fundamental mechanistic insights under operational conditions.

3.1. Cu C-SACs

CuN_4-based carbon nanocomposites are applicable as ORR catalysts in alkaline environments.[23,66] However, numerous recent investigations have indicated that the actual active sites of Cu-based C-SACs are the evolving structures of the CuN_4 moieties rather than the moieties themselves.[97–100] For instance, during the ORR process, a potential-driven transformation occurs from the initial $Cu–N_4$ to $Cu–N_3$, followed by HO–$Cu–N_2$ (Fig. 5a).[98] *Operando* characterization and DFT calculations have shown that the low-coordinated $Cu^+–N_3$ moiety acts as the true active site, exhibiting lower free energy in each elementary step compared with the $Cu^{2+}–N_4$ structure. Similarly, Fu and co-workers have clearly demonstrated the dynamic transition from $Cu–N_4$ to $Cu–N_4$/Cu-NC and subsequently to $Cu–N_3$/Cu-NC under ORR working conditions (Fig. 5b and c).[99] This sequential structural reconstruction phenomenon can effectively optimize the d-band center of the central metal and balance the energy of the OOH* and O* intermediates, thereby improving ORR activity. In addition, they also found that the atomic Cu sites within dual-metal Cu/

Fig. 5 (a) Schematic diagram of dynamic evolution of Cu−N₄ in ORR. Reproduced with permission.[98] Copyright 2023, American Chemical Society. (b) *Operando* XANES spectra and (c) Cu K-edge FT-EXAFS spectra of Cu−N−C/GC under the working condition. Reproduced with permission.[99] Copyright 2022, Wiley-VCH. (d) Schematic diagram of reversibly adapting configuration of CuNₓ in ORR. Reprinted with permission.[100] Copyright 2023, American Chemical Society. (e) Dynamic evolution of N-FeN₄C₁₀ under ORR conditions. Reproduced with permission.[102] Copyright 2020, Elsevier B.V. (f) The detailed ORR catalytic mechanism of Fe SAs/NSC in 0.1 M KOH. Reproduced with permission.[103] Copyright 2024, Wiley-VCH. (g) Scheme of *operando* XAF showing dynamic evolution of Fe−N₄ to Fe−N₂. Reproduced with permission.[104] Copyright 2021, American Chemical Society.

Zn C-SACs would undergo a reversible transition from CuN_4 to CuN_2, then to Cu clusters, and finally return to the initial CuN_4 under the applied electric field.[101] The rate-determining step would change from the formation of OOH* to OH* when the Cu−N coordination number changes from 4 to 2.

Surprisingly, the dynamic configurations of Cu SACs are related to micro-structural interface regulations. By using *operando* studies, Tan *et al.* found that the asymmetric CuN_3 sites in ZIF-derived Cu SACs underwent irreversible structural changes, in which the elongated Cu−N pair breaks during the ORR.[100] On the contrary, g-C_3N_4-derived Cu C-SACs with symmetric CuN_3 moieties were characterized by a reversibly adaptive nature under operational conditions, which led to their excellent ORR catalytic activity (Fig. 5d). These findings addressed the long-running controversy regarding real active sites for Cu C-SACs. This dynamic behavior of Cu C-SACs under realistic conditions suggested low-coordination CuN_x sites could be more active toward ORR by optimizing adsorp-

tion free energy of intermediates, guiding rational design principles for efficient C-SACs.

3.2. Fe C-SACs

Fe C-SACs are regarded as highly promising catalysts for ORR, with the Fe−N−C structures typically being viewed as the primary contributors to their ORR activity.[27] Nonetheless, even Fe C-SACs that share similar structural features may exhibit notable variations in their ORR/OER performances. Therefore, it is essential to clarify the reaction mechanisms and dynamic behavior of Fe C-SACs under electrochemical conditions to achieve optimal design. Li *et al.* identified three distinct types of Fe sites within Fe SACs—FeN_4C_{12}, FeN_4C_{10}, and N-FeN_4C_{10}—using *operando* [57]Fe Mössbauer spectroscopy.[102] The N-FeN_4C_{10} site, characterized by a five-coordinated structure, was determined to be highly active at elevated ORR potentials and exhibited a structural transformation to the N_4-plane upon the adsorption of O_2^- intermediates. At higher poten-

tials, the FeN_4C_{12} moiety served as the active sites, undergoing a dynamic shift away from the N_4-plane (Fig. 5e). Notably, the FeN_4 configuration was found to be the predominant characteristic of most as-synthesized Fe C-SACs. This raises the question of whether the FeN_4 moieties truly represent the active sites during the ORR. Pan's research group comprehensively explored the dynamic ORR mechanisms and the evolution of active porous Fe–N_4 sites using *in situ* ATR-SEIRAS, *in situ* Raman, *operando* XAS measurements, and theoretical calculations.[103] As shown in Fig. 5f, the active Fe sites evolved from a basic Fe–N_4 configuration to an active Fe–N_3 form by breaking the Fe–N bond under operational conditions, which aided in O_2 activation and enhanced the desorption of key intermediates (*OH). Furthermore, the Fe–N bond in Fe SACs could further fracture when a potential was applied. For example, the HO–Fe–N_4 species was dynamically converted to OH–Fe–N_2 with the breaking of two long Fe–N bonds, followed by the formation of an Fe–O coordination under ORR conditions (Fig. 5g).[104] This additional Fe–O bond was attributed to the chemical adsorption of key intermediates and the cleavage of the O–O bond within *OOH, contributing to a more efficient ORR process. The dynamic changes in Fe–N_x provide deeper insights into their active sites and the ORR mechanism.

3.3. Mn C-SACs

Mn, being a neighbor of Fe, possesses outer layer electrons configured as $3d^5 4s^2$. Recently, Mn C-SACs have garnered significant interest for their cost-effectiveness and high efficiency in electrocatalytic ORR/OER.[29,105] Nevertheless, due to the diverse chemical states and adjustable coordination structures of the Mn center, Mn C-SACs typically experience multiple forms of dynamic structural evolution throughout the intricate ORR/OER processes. For instance, *operando* XAS data combined with DFT calculations showed that as the applied potential increases, high-valence $Mn^{H+}–N^4$ can be progressively reduced to low-valence $Mn^{L+}–N_4$, which serves as the active site (Fig. 6a).[106] The $Mn^{L+}–N_4$ sites enhanced electron transfer to *OH species and promoted desorption of OH^-, thereby demonstrating superior electrocatalytic performance in the ORR. A similar real-time evolution of the local electronic structure of Mn SAC was documented by Shang *et al.* using *operando* X-ray absorption fine structure measurements.[38] DFT studies revealed that Mn–N_2C_2 sites offered better bifunctional ORR/OER activity compared with Mn–N_4 catalysts, as the distinct coordination environment could effectively modify the d-band center of Mn atoms. Observational data confirmed that the bond-length-extended $Mn^{2+}–N_2C_2$ moieties acted as genuine active centers during the ORR, while the bond-length-shortened high-valence $Mn^{4+}–N_2C_2$ moieties contributed to outstanding OER performance (Fig. 6b and c). Furthermore, Tong *et al.* elucidated the structural transformation of Mn–N_4 into Mn–N_3C and subsequently into Mn–N_2C_2 under the influence of applied potential through *operando* synchrotron radiation.[107] Concurrently, the valence states of Mn progressed from +3.0 to +3.8 and then decreased to +3.2. The formed $Mn^{+3.8}–N_3C$ and $Mn^{+3.2}–N_2C_2$ configurations could modulate

O_2 adsorption and lower the energy barrier for the rate-determining step (Fig. 6d–f). Mn SACs demonstrate remarkable bifunctional activity in both the ORR and OER processes. The substantial potential gap achieved by Mn SACs positions them as promising alternatives to noble metal-based catalysts.

3.4. Co and Ni C-SACs

Various studies indicated that CoN_4 sites are inclined to facilitate the production of H_2O_2 from O_2, while other research pointed to their preference for generating H_2O through a $4e^-$ transfer process.[111–113] Recent investigations have revealed that unsaturated-coordination CoN_x sites demonstrated superior bifunctional performance compared with CoN_4-based C-SACs.[114,115] Hence, it is essential to investigate the actual active sites and the underlying mechanisms of Co C-SACs. Liu *et al.* developed atomically coordination-regulated Co C-SACs featuring a five-coordinated Cl–Co–N_4 structure.[108] *In situ* characterizations have uncovered the dynamic transformation of the symmetry-broken Cl–Co–N_4 moiety into a coordination-reduced Cl–Co–N_2 structure, resulting in a decrease in d-band electron occupancy under working conditions for a fast $4e^-$ ORR (Fig. 6g).

Ni C-SACs with NiN_x configurations are generally known for their strong OER performance.[116] However, Cai *et al.* observed that the initial Ni–N coordination readily breaks down in the presence of adsorbed OH*, facilitating the stable formation of Ni–O, which acted as the true active center for OER (Fig. 6h).[109] Additionally, Zhang and colleagues found that the coordinated N within Ni–N–C was nearly entirely released as NO_3^- during the OER process, resulting in the rupture of the Ni–N bond.[110] The liberated Ni atoms ultimately form NiOOH nanoclusters, which serve as the genuine active sites for enhanced OER activity (Fig. 6i). Furthermore, Lou's group examined the potential-driven dynamic behavior of the Ni–N_4 sites during the OER, discovering that the Ni–N bond length decreased from 1.43 to 1.37 Å with an increase in the applied potential.[117] This finding suggested that electrocatalysts exhibiting stable activity may still experience certain reversible structural changes, which were crucial for catalytic kinetics.

4. Atomic-level regulation engineering

In oxygen electrocatalytic reactions, the exceptional conductivity and intrinsic activity of available sites within catalysts are key factors in achieving superior catalytic performance. To enhance the reaction rates theoretically, it is essential to optimize the adsorption and desorption energies of oxygen-containing species by fine-tuning the electronic structure of active sites.[27,66] Leveraging the structural flexibility of these sites, six atomic-level engineering strategies—namely modifying the coordination microenvironment, heteroatom modification, defect engineering, geometric distortion effect, dual-metal sites regulation, and guest groups strategy—play important roles in optimizing the electronic configuration of C-SACs.
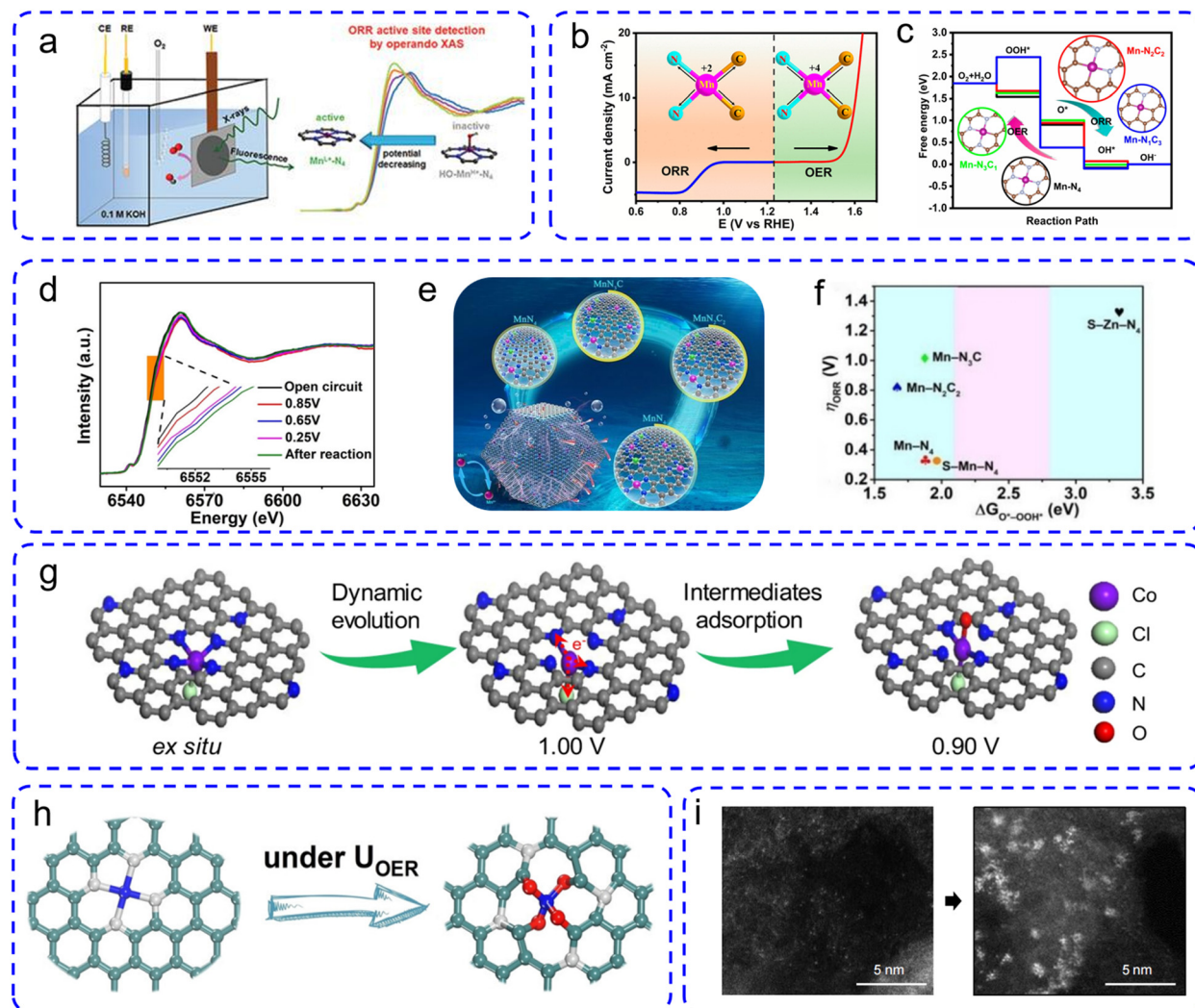
Fig. 6 (a) *Operando* X-ray absorption spectra characterizations. Reproduced with permission.[106] Copyright 2021, Wiley-VCH. (b) Schematic diagram of dynamic evolution of Mn–N$_2$C$_2$ moieties under ORR/OER. (c) Theoretical ORR and OER activity of Mn SAC. Reprinted with permission.[38] Copyright 2020, American Chemical Society. (d) Mn K-edge XANES spectra at different applied potentials. (e) Schematic diagram of dynamic evolution of Mn SAC. (f) The $\Delta_{GO*-OOH*}$ and η_{ORR} values of different models. Reproduced with permission.[107] Copyright 2023, Wiley-VCH. (g) ORR schematics of CR-Co/ClNC. Reprinted with permission.[108] Copyright 2024, Springer Nature. (h) The deduced evolution pathway of single-atom catalyst. Reproduced with permission.[109] Copyright 2024, Wiley-VCH. (i) Transformation of Ni in Ni–N–C during activation. Reproduced with permission.[110] Copyright 2024, Wiley-VCH.

These atomic-level regulation strategies can deepen our understanding of the mechanism for enhancing catalytic performance and further offer important guidance for building efficient bifunctional C-SACs.

4.1. Regulating the coordination microenvironment

There is a general consensus that metal atoms are stabilized within the carbon matrix through bonding with coordination atoms, with their electronic structures being significantly influenced by the surrounding the coordination microenvironment. Typically, a single metal atom (M) directly coordinates with four N atoms to form a planar symmetric MN$_4$, which restricts the enhancement of the oxygen electrocatalytic activity. However, by adjusting the type or number of coordi-

nation atoms—through their differing electronegativities—it is possible to disrupt this symmetry and optimize the electron cloud arrangement of the central metal atoms, thereby influencing its adsorption and desorption characteristics.

4.1.1. Changing the type of coordinated atom. This optimization is realized through deliberately substituting one or more N atoms within the MN$_4$ site to form M–X (X = O, S, P, *etc.*) bonds with central metal atoms. In the situation of heteroatoms replacing N atoms of MN$_4$, the P, S, and B heteroatoms with lower electronegativity than N atoms would lower valence states of central metal atoms.[68,118,119] Conversely, higher electronegativity heteroatoms (*e.g.* F, O) would obtain electrons from single metal atoms.[48,49] Recent studies have shown that C-SACs with MN$_y$X$_{4-y}$ moieties display enhanced

oxygen electrocatalytic activity compared with those with only MN$_4$ sites.[50,120] Guan *et al.* comparatively researched two types of graphene-supported Co SACs with different coordination structures (Fig. 7a).[72] The experimental results indicated that the Co$_1$/BNG catalyst with Co–N$_3$B sites exhibited better ORR/OER activity than Co–N$_4$ sites. Results from *in situ* spectral characterization indicated that B incorporation can promote the protonation of *O$_2$ and increase the adsorption energy between the central Co atom and *OOH. The DFT calculations also revealed that the enhanced oxygen electrocatalytic per-

formance benefited from an upward shift d-band of the Co atom induced by the modification of B atoms, resulting in a stronger overlap of Co-d and O-p orbitals near the Fermi level. It is evident that the electron accumulation reduced the valence state of the Co sites and thus improved ORR activity. This phenomenon is strongly supported by prior studies on Cu SACs, where the chemical state of Cu atom within CuS$_1$N$_3$ moiety was regulated by introducing coordinated sulfur atom.[121] Significantly, the CuS$_1$N$_3$ sites, characterized by low valence (+1) and shortened Cu–N bonds due to dynamic evol-
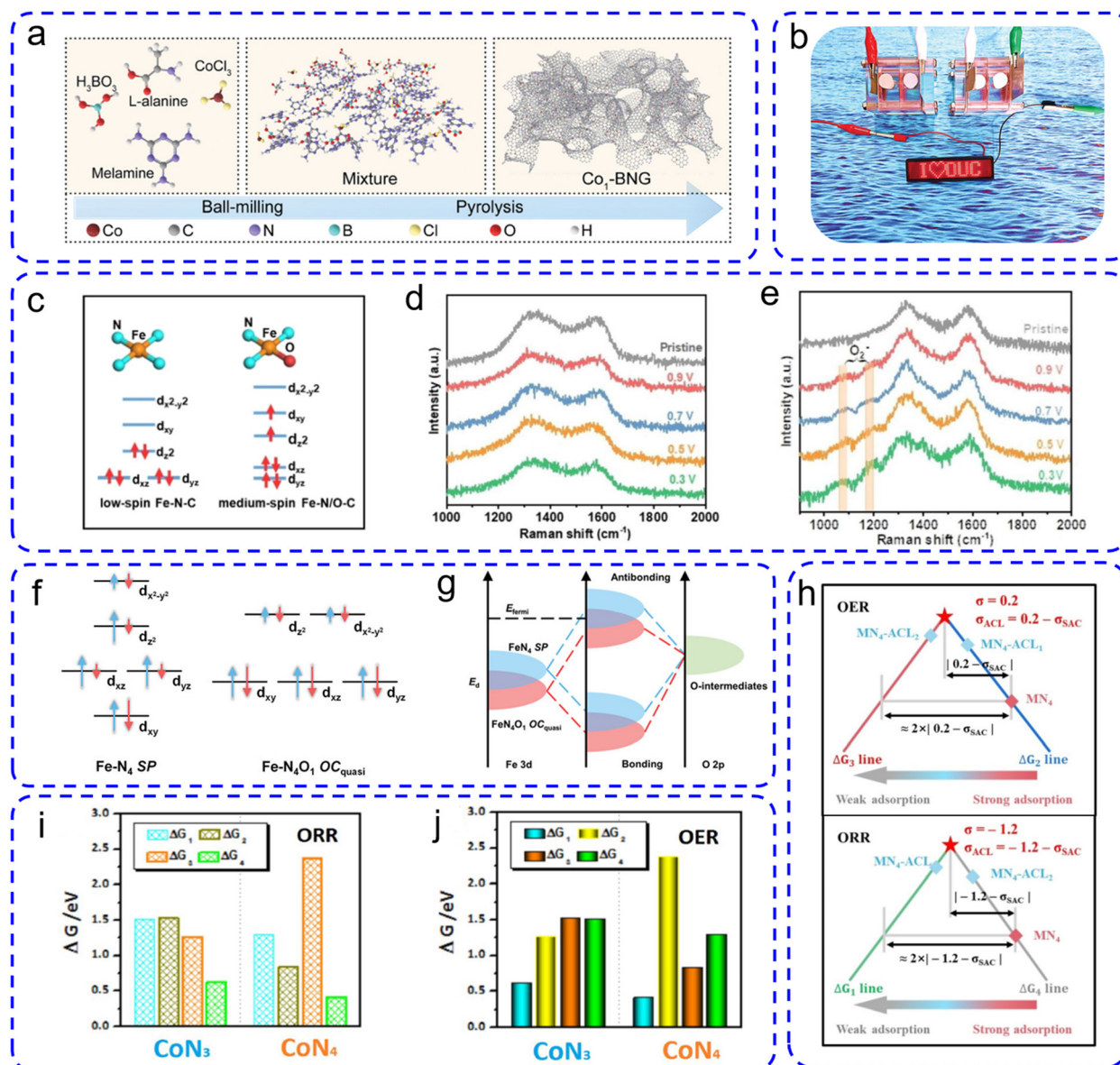

Fig. 7 (a) Schematic of the synthesis of Co$_1$-BNG. Reproduced with permission.[72] Copyright 2024, Wiley-VCH. (b) The red light-emitting diode screen powered by two seawater-based ZABs in tandem. Reproduced with permission.[122] Copyright 2022, Wiley-VCH. (c) Schematic diagram of d-orbital spin-electron filling states. *In situ* Raman spectra of (d) Fe–N–C and (e) Fe–N/O–C. Reproduced with permission.[123] Copyright 2024, Wiley-VCH. (f) Schematic diagram of the modulation of d-orbital splitting manner. (f) Schematic of the optimized bonding behavior. Reproduced with permission.[125] Copyright 2023, Wiley-VCH. (h) Diagram of optimal range of σ for ACL decoration for OER (top) and ORR (bottom). Reproduced with permission.[126] Copyright 2024, Wiley-VCH. The calculated ΔG in each step of (i) OER and (j) ORR process for both models. Reproduced with permission.[127] Copyright 2024, Elsevier B.V.

ution, were identified as the actual active centers for ORR through *in situ* XAS measurements. Furthermore, research by Wang *et al.* indicated that P doping in the atomically asymmetric Co–N$_3$P–C structure could modify the electronic properties of the Co sites, resulting in a lower charge for Co atoms in the Co–N$_3$P–C model compared with the Co–N$_4$–C model.[122] The asymmetric Co–N$_3$P–C sites, which possessed symmetry-breaking electronic structures, enhanced the affinity for strong OH$^-$ and weak Cl$^-$ adsorption, demonstrating their potential for practical applications in seawater-based ZABs (Fig. 7b).

Highly electronegative heteroatoms can also adjust the d-band electronic configuration and spin state of the central metal atom, thereby in turn improving the ORR/OER activities.[49] Li *et al.* synthesized a catalyst featuring N,O-codoped carbon skeleton-supported single Fe atoms (Fe–N$_3$O–C) by using an *in situ* pyrolysis strategy.[123] Importantly, the asymmetric coordination of oxygen around the iron atom changed the d-orbital energy and facilitated a transition from low-spin Fe^{2+} to medium-spin Fe^{2+} (Fig. 7c). The latter's unpaired electrons in the d$_{z^2}$ orbitals can engage with the antibonding π* orbitals of oxygen intermediates, thus preventing excessive adsorption. Furthermore, a combination of DFT calculations and *in situ* Raman spectral analysis revealed that the rate-limiting step of asymmetric Fe–N$_3$O sites shifted from the *OH desorption to the hydrogenation of O$_2$* compared with the symmetric Fe–N$_4$ sites, leading to a substantial enhancement in ORR activity (Fig. 7d and e). In brief, both electron-donating and electron-withdrawing heteroatoms can regulate the electronic structure of the metal center atom in MN$_y$X$_{4-y}$ moieties. Notably, the oxygen electrocatalytic activity can be significantly improved by precisely choosing the central metal atom and coordination heteroatoms with appropriate electronegativity.

4.1.2. Changing the corrdination number of the metal atom. Besides substituting N atoms with other heteroatoms, adjusting the coordination number is also a versatile method to directly tune electronic configuration of active metal sites.[67,124] Previous reports indicated that an axial heteroatom could bond the MN$_4$ moieties to form five-fold coordinated metal sites, thus restructuring the d-orbital level of the central metal atom.[128,129] Dai *et al.* successfully designed and synthesized a single-atom Fe catalyst (Fe–N$_4$O$_1$ OC) with planar FeN$_4$ moieties bonding with one axial O atom out of plane.[125] Compared with Fe–N$_4$ sites, the axial O ligand could lead to the distortion of the local crystal field and spin polarization of the central Fe atom from square-planar coordination with intermediate-spin state to a quasi-octahedral field with low-spin state (Fig. 7f and g). The decrease in the number of unpaired electrons in d$_{z^2}$, d$_{xz}$ and d$_{yz}$ orbitals could facilitate desorption of *OH, thereby boosting the reaction activity. As a result, the ZABs constructed with such Fe–N$_4$O$_1$ OC electrocatalyst could provide a P_{max} of 191.5 mW cm^{-2}. In fact, numerous studies have shown that the axial coordination ligands (ACLs) can additionally disperse d-orbital electrons of the metal atom and lower the adsorption capability of them.[128,130,131] Qiao *et al.* systematically studied more than 100 types of ACL-SACs randomly combining with transition metals and ten kinds of

ACLs by means of large-scale DFT computations.[126] Notably, a general structure descriptor σ jointly decided by electronegativity and the number of valence electrons was constructed for predicting the catalytic performance of the ACL-SACs (Fig. 7h). The CrN$_4$-, FeN$_4$-, CoN$_4$-, RuN$_4$-, RhN$_4$-, OsN$_4$-, IrN$_4$- and PtN$_4$-ACLs were considered to possess higher activities than Pt and IrO$_2$ catalysts for both ORR and OER.

In addition, reducing the coordination number is also an effective method to regulate the electronic structure of the central metal and improve the ORR/OER activity of C-SACs. Xiao *et al.* recently predicted that the asymmetric M–N$_3$ sites should have superior bifunctional activity to M–N$_4$ sites, because more unpaired free electrons occupy the d orbitals of the M–N$_3$ sites and can additionally interact with p orbitals of ORR/OER intermediates.[132] Previous studies also indicated that both bi-coordinated and tri-coordinated sites have implied better ORR/OER activity than tetra-coordinated sites owing to the asymmetric electronic structure of the former.[98,114,133] Liu *et al.* fabricated the N-doped carbon-nanotube embedded with unique Co–N$_3$ sites (CoSA-NLF) as bifunctional ORR/OER electrocatalysts.[127] Compared with Co–N$_4$ sites controlled by the generation of O* with the energy barrier of 1.14 V, the rate-determining step of Co–N$_3$ site was transformed into the generation of OOH* (ΔG = 0.30 V) during the OER process. Moreover, the dissociation energy barrier of *OH in Co–N$_3$ sites was lower than Co–N$_4$ sites during the ORR process (Fig. 7i and j). The DFT calculations indicated that the low-coordinated Co–N$_3$ sites with more obvious spin polarization than Co–N$_4$ sites could optimize the adsorption/desorption processes of the oxygen-containing intermediates. Interestingly, some as-synthesized M–N$_4$ structures could also transform into low-coordinated active sites under the working conditions. For example, the original Cu–N$_4$ sites would transform into the unsaturated Cu–N$_3$ as the real reaction sites to reduce the ORR reaction energy barrier, as assessed through *in situ* XANES spectroscopy.[98]

The above results convey a profound understanding of the local coordination effect of C-SACs. Constructing asymmetric MN$_y$X$_{4-y}$ structures is the key to optimizing the electronic configuration of central metal atoms for boosting the ORR/OER catalytic activities of C-SACs. In other words, regulating the coordination microenvironment of C-SACs is significant for achieving advanced bifunctional catalysts for highly efficient R-ZABs.

4.2. Heteroatom modification

In contrast to the addition of heteroatoms (P, S, B, N, *etc.*) within the primary coordination shell of metal atoms, heteroatom modification involves integrating these atoms into the lattice of carbon substrates. This integration disturbs the electronic configuration of the central metals *via* long-range interactions.[124,134] It is widely recognized that the presence of heteroatoms can also lower charge transfer resistance and significantly improve the hydrophilicity of carbon substrates.[135,136] Optimization of these surface/interface physicochemical properties could collectively boost oxygen electro-

catalytic activity of C-SACs. Yang *et al.* successfully revealed the pivotal role played by S doping for enhancing ORR/OER activities by fabricating S-doped carbon fiber membrane with FeN$_4$ moieties.[137] The S modification would reduce the desorption energy of *OH during ORR process and the formation energy of *OOH during OER process in the FeN$_4$ sites, therefore contributing to boosting the bifunctional activities. The obtained R-ZAB exhibited a large peak power density of 255.84 mW cm^{-2} and excellent stability of 1000 h. Notably, recent research has shown that the S atoms within a carbon skeleton could induce the formation of other oxygen functional groups to mutually decorate single atom sites. Zhao *et al.* optimized the ORR energy barrier of atomically dispersed FeN$_4$ sites within

carbon substrates by doping S atoms (Fig. 8a and b).[138] The S group and induced epoxy group jointly modulated the spin state of the Fe orbital and effectively enhanced the charge transport, therefore facilitating desorption of OH*. The as-synthesized catalyst displayed a higher $E_{1/2}$ of 0.92 V, which was much better than that of commercial Pt/C catalyst. Besides, due to the different electronegativity from C atoms, heteroatoms may also distort the local electric field and furthermore influence the electronic structure of metal reactive centers.[139,140] As shown in Fig. 8c, external electron-donating pyrrolic-N (PN) near FeN$_4$ sites could evoke the local electrical field and positive charge aggregation on Fe atoms.[141] Compared with the FeN$_4$ sites, the local electric field of FeN$_4$-
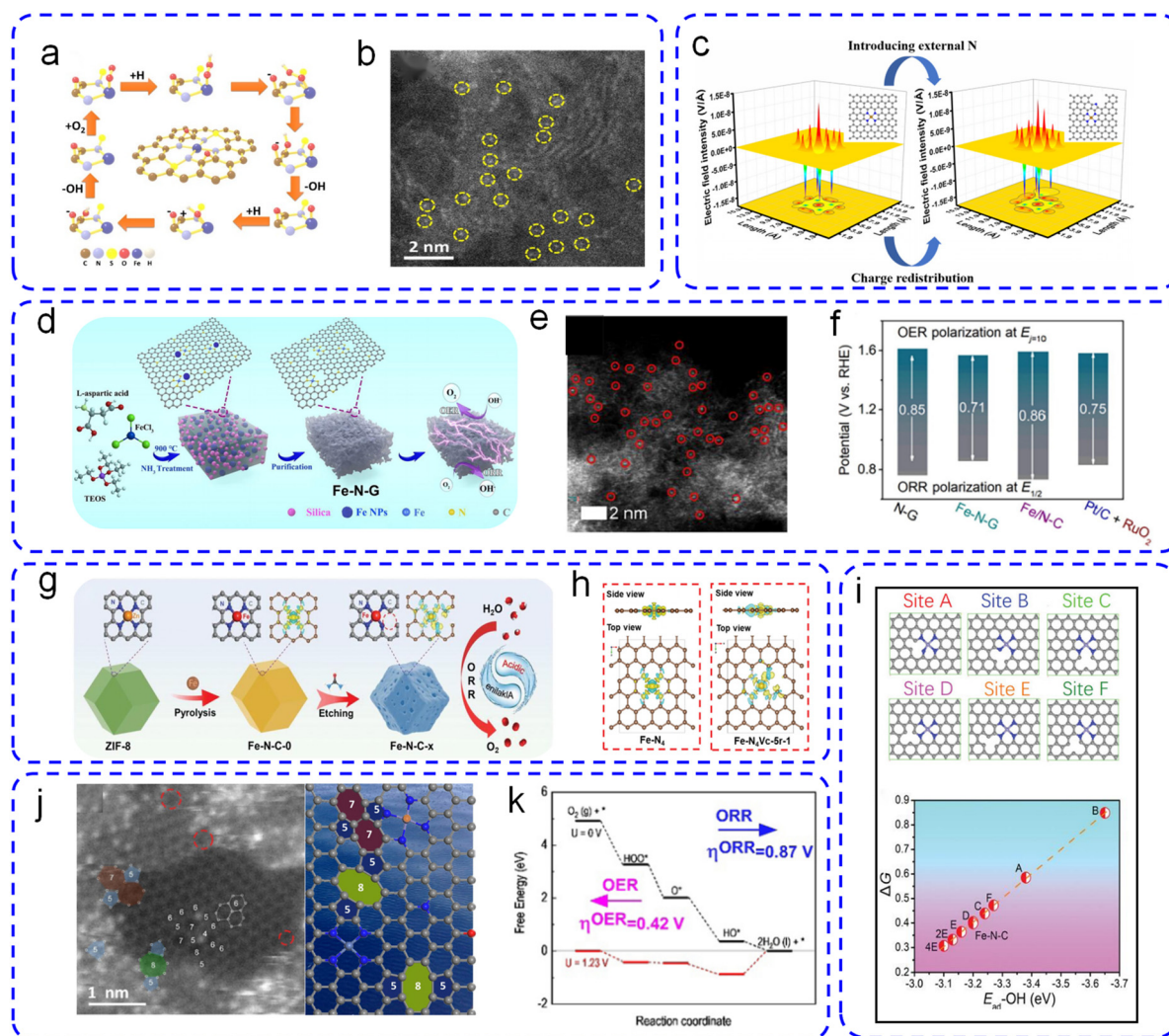

Fig. 8 (a) Mechanism illustration of epoxy groups participating in ORR process. (b) HAADF-STEM images of Fe$_1$/NSOC. Reproduced with permission.[138] Copyright 2023, Wiley-VCH. (c) MATLAB simulations of local electric field on FeN$_4$ (left) and FeN$_4$-PN (right) in two dimensions. Reprinted with permission.[141] Copyright 2021, American Chemical Society. (d) The fabrication procedure and (e) HAADF-STEM images of Fe−N−G. (f) The potential gaps of different catalysts. Reproduced with permission.[148] Copyright 2023, Elsevier B.V. (g) Schematic of the synthesis strategy of Fe−N−C. (h) The computed differential charge density between Fe−N$_4$ and Fe−N$_4$Vc-5r-1. Reproduced with permission.[149] Copyright 2023, Wiley-VCH. (i) The relationship between the adsorption energy of OH* and the ΔG of potential determining step on Fe−N−C with six C vacancies. Reproduced with permission.[150] Copyright 2023, Wiley-VCH. (j) Illustration of a proposed model composed of different C atoms' coordination with Ni/Fe single atoms. (k) Free energy diagram calculated for ORR and OER with 5775 defects. Reproduced with permission.[151] Copyright 2021, Elsevier B.V.

PN sites was twisted and asymmetrical, resulting in enhanced charge circulation. Therefore, more electrons in FeN$_4$-PN sites could readily transfer from Fe d$_{z^2}$ to the O$_2$ p$_z$ orbital for sufficient activation of O$_2$, significantly enhancing the ORR process. Therefore, reasonable heteroatom modification can improve performance by adjusting conductivity, intermediate adsorption energy and other aspects.

4.3. Defect engineering

Defect engineering is a well-accepted method for modifying the electronic structure of C-SACs. In general, defect sites in C-SACs include inherent carbon defects (such as edges, vacancies or topological defects) and extrinsic defects introduced by the heteroatoms.[142,143] While many studies focused mainly on heteroatom doping, they often overlooked the role played by inherent defects in improving the electrocatalytic performance of C-SACs. In the previous subsection, we have thoroughly discussed the regulatory effect of heteroatom modification on the electronic structure of C-SACs. Here, we primarily discuss how inherent carbon defects contribute to improving the electrocatalytic ORR/OER performance. Generally, surface defects can effectively modify the local electronic distribution of central atoms and increase the orbital hybridization, thereby optimizing intermediate adsorption strength and promoting electron transfer.[144,145] It is acknowledged that the catalytic activity of metal sites located at the edge surpasses that of those situated on the basal plane.[146–148] As an example, Gan and co-workers found that porous graphitic carbon with edge Fe–N$_x$ sites exhibited a higher $E_{1/2}$ of 0.86 V in ORR and a lower E_{10} of 1.57 V in OER compared with in-plane Fe–N$_x$ sites (Fig. 8d–f).[148] The improvement of bifunctional performance stemmed from the edge Fe–N$_x$ site being superior to the in-plane Fe–N$_x$ site regarding accelerating OH* dissociation in ORR and OOH* formation in OER. Carbon vacancies or pores mean the deletion of carbon atoms on the sp^2-conjugated carbon plane, which is another common inherent defect in C-SACs.

Actually, the edges mentioned above often appear with the vacancies/pores on the substrate surface.[143] Therefore, the influence of vacancies/pores is analogous to that of edges. Tu's group explored the impact of adjacent carbon vacancy on FeN$_4$ active sites by fabricating atomically dispersed Fe–N–C catalyst with carbon defects (Fe–N$_4$–Vc) (Fig. 8g).[149] DFT calculations demonstrated that both electron redistribution on the defect surface and more positive charges near the Fe site caused by the vacancy could distort charge distribution and reduced Fe state, thus lowering the *OH desorption energy barrier during the ORR process (Fig. 8h). The R-ZABs constructed with such Fe–N$_4$–Vc electrocatalyst could supply a P_{max} of 218 mW cm^{-2} and excellent stability of 200 h. Notably, the different types of carbon vacancies near metal sites will lead to different ORR kinetics.[150] As shown in Fig. 8i, the mixing between Fe-3d and O-2p for Fe–N–C with site E became weakest, resulting in moderate adsorption of OH* and thus enhancing the electrocatalytic ORR activity. In addition to improving intrinsic activity, vacancies/holes can also serve as a "trap" for stabilizing single metal atoms and facilitate rapid electron/mass transfer.[152,153] Up to now, various technologies including the template method, plasma etching and alkaline activation have been used to optimize the hierarchically porous structure with appropriate vacancy defects.[153–155]

Interestingly, non-hexagonal topological defects, such as pentagonal, heptagonal, and octagonal structures in carbon substrates, also serve as a significant factor influencing the intrinsic reaction activity of the MN$_x$ sites.[151,156,157] For example, the Fe–N$_4$@Ni–N$_4$ moieties embedded on carbon substrates with the abundant Stone–Wales (SW) defect (pentagon–heptagon–heptagon–pentagon, 5775 defects) displayed enhanced OER activity relative to the pristine Fe–N$_4$@Ni–N$_4$ sites (Fig. 8j).[151] The SW defects could weaken the resonance stabilization among the sp^2 atoms and promote the charge accumulation on metal atom sites, thus accelerating O* transformation to OOH* (Fig. 8k). In short, careful design of the defects at the surface/interface of C-SACs can effectively optimize the electronic structure of active sites, which is thought to be one of the most promising strategies to improve the bifunctional catalytic performance.

4.4. Geometric distortion effect

Notably, in the majority of the earlier reports, the carbon substrate enriched with M–N$_x$ sites was usually assumed as a two-dimensional planar model, although nonplanar/distorted nanostructures are common in carbon skeletons.[67,112,158] Several significant issues arise here. Will the electronic structure vary when the metal atoms are embedded in distorted and flat carbon support? Can the curvature regulation of the carbon substrate enhance bifunctional catalytic activity of M–N$_x$ sites? In a recent study, Tan et al. designed and prepared Zn–N$_4$ moieties supported on a surface-bent spherical carbon support (S–Zn–N–C) as an oxygen electrocatalyst with a high $E_{1/2}$ of 0.89 V (Fig. 9a).[159] The DFT calculations and characterizations displayed that geometric bending could change the Zn–N bond length and induce more electron transfer from the 3d orbital of Zn^{2+} to the surrounding N atom, therefore optimizing the adsorption strength to critical oxygen intermediates. Furthermore, because the degree of electron redistribution can be efficiently regulated by the curvature, Zn–N$_4$ sites supported on the carbon substrate with 30–45° bending angle suggested the optimal ORR activity. In the case of the S–Zn–N–C-based aqueous ZABs, a P_{max} of 229.2 mW cm^{-2} and excellent stability of 300 h were achieved (Fig. 9b).

Similarly, through using quantum mechanics and machine learning Kang et al. obtained the conclusion that there was a linear downshift of the energy level of the Fe d-orbital as curvature increased, and thus ORR activity improved by decreasing the energy barrier of the potential-determining step.[163] In addition, studies have also found that the high strain resulting from a curved substrate was potentially released by forming additional M–O bonds to distort the conjugated framework. For example, the reason for the CuN$_2$C$_2$ site in wrinkled carbon with enhanced ORR activity was that the axial Cu–O bond induced by distortion facilitated the charge transfer from
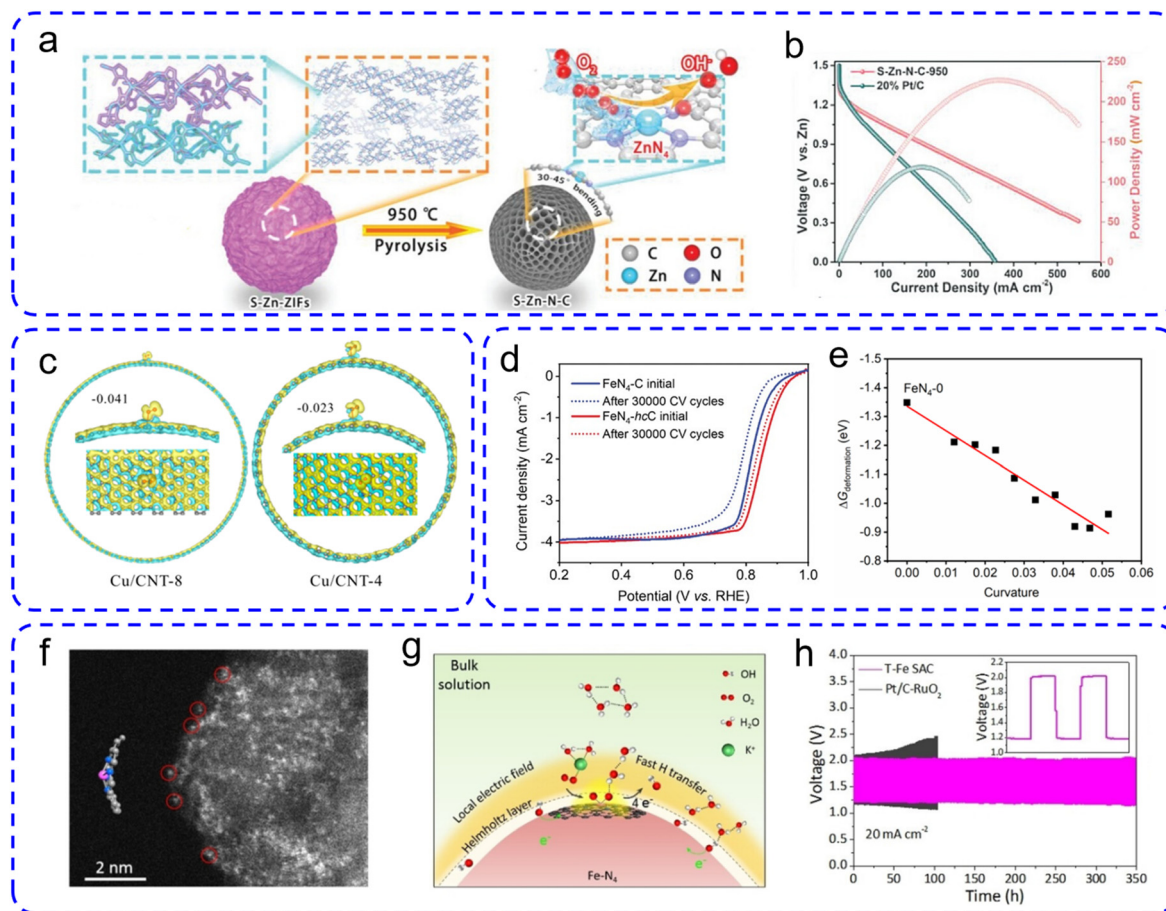
Fig. 9 (a) Schematic diagram of the preparation of S–Zn–N–C. (b) Power density curves corresponding to the discharge voltage curves. Reproduced with permission.[159] Copyright 2024, Wiley-VCH. (c) Side view and top view of the charge density difference for three models with O_2^*. Reproduced with permission.[160] Copyright 2021, Springer Nature. (d) ORR polarization curves for different catalysts before and after 30 000 CV cycles. (e) Correlations between $\Delta G_{\text{deformation}}$ of the FeN_4 site with the curvature. Reproduced with permission.[161] Copyright 2023, Wiley-VCH. (f) HAADF-STEM image of T-Fe SAC. (g) A schematic showing the ORR microenvironment. (h) Charge–discharge curves. Reproduced with permission.[162] Copyright 2024, Wiley-VCH.

Cu to the adsorbed oxygen species (Fig. 9c).[160] In addition to improving reaction activity, the stability of FeN_4 sites on the curved carbon heightened with the increasing curvature (Fig. 9d and e).[161] The deformation of FeN_4 sites is the key factor for determining the stability of Fe-based single-atom catalysts.

In particular, the tips exhibit the greatest curvature. Early research studies have shown that the tip structure often existing in metal nanoneedle/nanocone arrays could generate a localized electric field, inducing the accumulation of intermediate.[164–166] Wang *et al.* successfully synthesized the tip-like Fe–N_4 sites (T-Fe SAC) on spherical carbon surfaces *via* the "assembly–electrospray–pyrolysis" gradual strategy, exhibiting exceptional ORR/OER activity (Fig. 9f).[162] Different from the end-on mode in planar Fe sites, the adsorption of O_2 molecules at the tip-like Fe sites followed the side-on mode. The orbitals of O_2 interact tightly with d_{xz} and d_{z^2} orbitals in T-Fe SAC, thus greatly weakening σ bonding and facilitating O–O bond dissociation. Moreover, the strong local electric field

caused by tip-like FeN_4 increased the density of the water layer and weakened hydrogen bonding interaction, thereby enhancing the electron-coupled proton transfer process (Fig. 9g). Using T-Fe SAC as an air cathode in liquid ZABs, a high $P_{\max}$ of 199 mW cm^{-2}, a specific capacity of 803 mA h g^{-1}, and a small ΔE of 0.85 V were realized (Fig. 9h). These findings emphasize the significant role played by high-curvature nanostructures and encourage the thoughtful design of more sophisticated C-SACs for the ORR/OER by leveraging this geometric distortion effect.

4.5. Dual-metal site regulation

Because of the different requirements of ORR and OER for active sites, most carbon-based M–N_x sites may only show good single function for ORR or OER.[28] Zheng *et al.* studied the intrinsic ORR activity of different metal atoms in N-doped carbon and ultimately confirmed the trend of Fe > Co > Mn > Ni.[167] Correspondingly, Fei *et al.* discovered that the OER activities of MN_4C_4 moieties follow the sequence of Ni > Co >

Fe.[116] Hence, constructing dual-metal sites is expected to exert complementary functionalities or synergistic effects toward ORR and OER. Simultaneously, the strong metal–metal interactions can disturb the electronic structures of active metal centers, resulting in charge difference and spin polarization.[70,168] Dual-metal sites are generally classified into two categories, depending on whether the two metal atoms are coordinated by heteroatoms separately or jointly. Specifically, in the first category, two metal atoms are coordinated by heteroatoms independently dispersed into the carbon matrix without any metal–metal connections.[169–171] In contrast, the second category features a direct bonding site between M_1 and M_2.[168,172] Up to now, a variety of carbon-based dual-atom site catalysts, such as bimetallic Fe/Mn,[173] Fe/Co,[174] Co/Ni,[169] Fe/Cu,[71] Co/Cu,[175] etc., have been explored for the role they can play as bifunctional oxygen catalysts.

In the first type of dual-metal site mentioned above, there is hardly any electronic interaction between the adjacent $M–N_x$ sites if they are far apart in the carbon skeleton. For instance, $Fe–N_4$ and $Ni–N_4$ sites located in the outer and inner walls of nanospheres did not mutually interfere and only contributed to high activity toward ORR and OER, respectively.[170] It is generally agreed that the electronic configuration of M_1-N_x and M_2-N_x may influence each other by long-range interactions when the inter-nuclear distance diminishes by several angstroms.[176,177] He et al. prepared FeN_4–CuN_4 dual-sites supported on a N-doped carbon aerogel (NCAG/Fe–Cu) as a bifunctional ORR/OER catalyst with a low ΔE of 0.67 V.[71] The distance between Fe–Cu atomic pairs is approximately 5.1 Å. Hence, the adjacent Cu atom as an electronic regulator could decrease the Fe magnetic moment within the FeN_4 moieties via increasing the electron density of the Fe d_{z^2} orbital, which optimized the adsorption energy of *OH intermediates (Fig. 10a). Notably, a quasi-solid ZAB integrated with NCAG/Fe–Cu could offer a P_{max} of 186 mW cm^{-2} (Fig. 10b) and stability for over 800 cycles. It is worth noting that the relative position of the metal center within dual-metal sites may change during electrocatalytic processes. As shown in Fig. 10c, NiFe-CNG could undergo structural evolution to dynamically form the Ni–Fe dual-sites bridged with two oxygen atoms, resulting in the emergence of a spin channel and the further improvement of OER activity.[178]

When M_1–N_x and M_2–N_x draw close and share two coordinating atoms to form the N_2M_1–N_2–M_2N_2 configuration, a suitable distance between M_1 and M_2 may enable a bridge-adsorption mode for O_2 and facilitate the direct breakage of O–O bonds, thus improving the ORR reaction kinetics.[179–181] Importantly, metal bonds could also occur in dual-metal C-SACs to form "real" dual-metal sites. In this situation, there is a strong electronic interaction between M_1 and M_2 via metal–metal charge transfer (MMCT) and orbital hybridization.[168,182–184] Wang's group reported the synthesis of Fe–Co dual sites embedded in O, N co-doped carbon nanosheets (FeCo–N_3O_3@C), displaying exceptional ORR/OER activities with an ultra-low ΔE of 0.59 V.[184] The strong coupling of the Fe–N_3 and Co–O_3 moieties reshaped the filling of the 3d

orbitals of the Co and Fe atoms, optimizing the adsorption–desorption of the reaction intermediates and effectively improving the reaction kinetics of both ORR and OER. The liquid ZABs with FeCo–N_3O_3@C displayed a P_{max} of 143 mW cm^{-2}, high specific capacities of 787.2 mA h g^{-1} and long-term stability over 200 h. As shown in Fig. 10d, an LED scroller was powered by three ZABs in series, affirming the potential application of FeCo–N_3O_3@C in energy storage devices.

The results from these research studies manifested that the complementary or synergistic effects originating from dual-metal sites can considerably boost oxygen electrocatalytic activities. Excitingly, the dual-metal sites can hopefully improve the stability of C-SACs. A second metal element may inhibit carbon substrate corrosion and also alleviate demetalation of active MN_x sites through electronic interactions. Hu et al. found that Mn atoms could induce an electron delocalization effect in d orbitals of the Fe center to reduce the oxidation state of Fe, thereby improving the strength of the Fe–N bond (Fig. 10e–g).[181] The synthesized FeMn–N–C catalysts achieved an ultralong cycling stability of 700 h in R-ZABs. A recent study has also shown that the Mn atoms could effectively scavenge the attack of oxygen radicals for Fe–N_x sites for improvement in ORR durability.[173] However, there are huge challenges to reach precise control of the construction of dual-metal sites. Further efforts are necessary for screening high-performance dual-metal pairs and monitoring the dynamic behavior of the active sites. Despite the advancements aimed at enhancing the stability of C-SACs and prolonging the lifespan of R-ZABs, a cycle life of merely a few hundred hours remains inadequate for the commercial viability of R-ZABs. Recently, the Lv group introduced a dual-metal site catalyst (CuNa-CF), featuring Cu–N_4 sites and Na-containing functional groups encapsulated in carbon nanofibers.[42] As illustrated in Fig. 10h, the Cu-3d orbitals exhibited greater overlap with *OOH intermediates following the modification with –COONa functional groups. Furthermore, the presence of Na-containing functional groups significantly diminished the positive charge on nearby C atoms, making the carbon substrates less prone to degradation by oxygen species and enhancing the stability of Cu–N_4 sites. As depicted in Fig. 10i, the assembled R-ZAB utilizing CuNa-CF demonstrated exceptional discharge and charge cycle stability for over 5000 h, supplying insights into the strategic design of commercially viable R-ZABs.

4.6. Guest groups strategy

Similar to dual-metal site regulation, introducing additional nanoparticles including metals and their derived carbides, phosphides, oxides, etc. to tune the catalytic behaviour of C-SACs is known as "guest group strategy". It is generally acknowledged that single metal atoms within a carbon substrate show ultrahigh ORR activity, while nanosized metal species contribute to improving the OER performance.[30,185,186] Moreover, the nanoparticles can effectively tune the electronic structure of the atomically dispersed metal sites through long-range interactions.[187–189] Hence, it would be a better choice to overcome the inherent shortcoming of single-function C-SACs
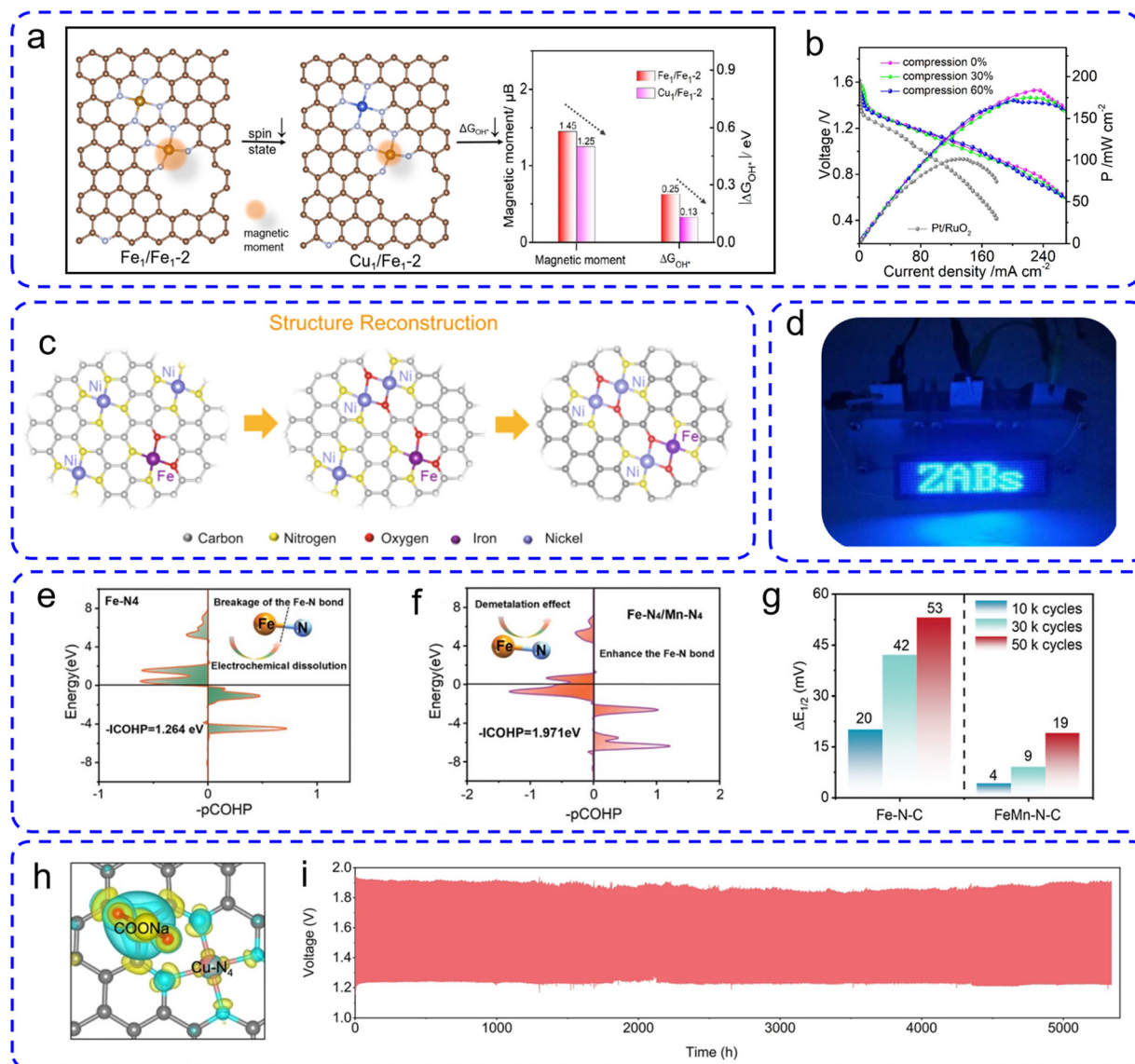
Fig. 10 (a) Schematic illustration of the moderating effect of magnetic moment on ΔG_{OH*} for the bimetal sites at the nanopore. (b) Discharge polarization and the corresponding power density curves. Reproduced with permission.[71] Copyright 2022, Wiley-VCH. (c) Structural reconstruction of NiFe-CNG during OER. Reprinted with permission.[178] Copyright 2022, American Chemical Society. (d) Optical image of an LED powered by three Zn//FeCoN$_3$O$_3$ batteries in series. Reprinted with permission.[184] Copyright 2024, Springer Nature. (e) Scheme of the relationship between structure–activity-potential. COHP analysis and the corresponding ICOHP values of the Fe–N bond in (e) Fe–N$_4$ and (f) Fe–N$_4$/Mn–N$_4$. (g) The half-wave potential degradation after different cycle numbers of CV. Reproduced with permission.[181] Copyright 2024, Wiley-VCH. (h) Charge density differences of Cu–N$_4$-COONa. (i) Discharge/charge cycling curves of Zn//CuNa-CF battery. Reprinted with permission.[42] Copyright 2024, Springer Nature.

via constructing hybrid components. For example, a nanocomposite consisting of Fe single-atom sites and neighboring Fe clusters (Fe$_{SA/AC}$@HNC) was successfully prepared as an excellent oxygen electrocatalyst for R-ZABs (Fig. 11a).[188] As shown in Fig. 11b, the additional Fe clusters contributed to the rearrangement of the 3d orbital electrons and induced the electron spin-state transition from the low spin (LS, $t_{2g}^6 e_g^0$) to the medium spin (MS, $t_{2g}^5 e_g^1$) in FeN$_4$ moieties, thereby reducing the binding strength of *OH and in turn improving the ORR activity. The Fe$_{SA/AC}$@HNC delivered a high P_{max} of

171.5 mW cm^{-2} (Fig. 11c) and good charging and discharging performance with a narrow gap of 0.85 V in R-ZABs.

It is worth noting that metal clusters may reversibly convert into oxyhydroxides under high potential conditions. As a typical example, Ding *et al.* found that the Co nanoparticles within a Co-CoN$_4$ hybrid would dynamically transform into active CoOOH at high potentials to further enhance the OER activity (Fig. 11d).[185] More importantly, it is a rational method for improving the chemical stability of single-atom metal sites by coupling nanoparticles. For instance, Zhang's group
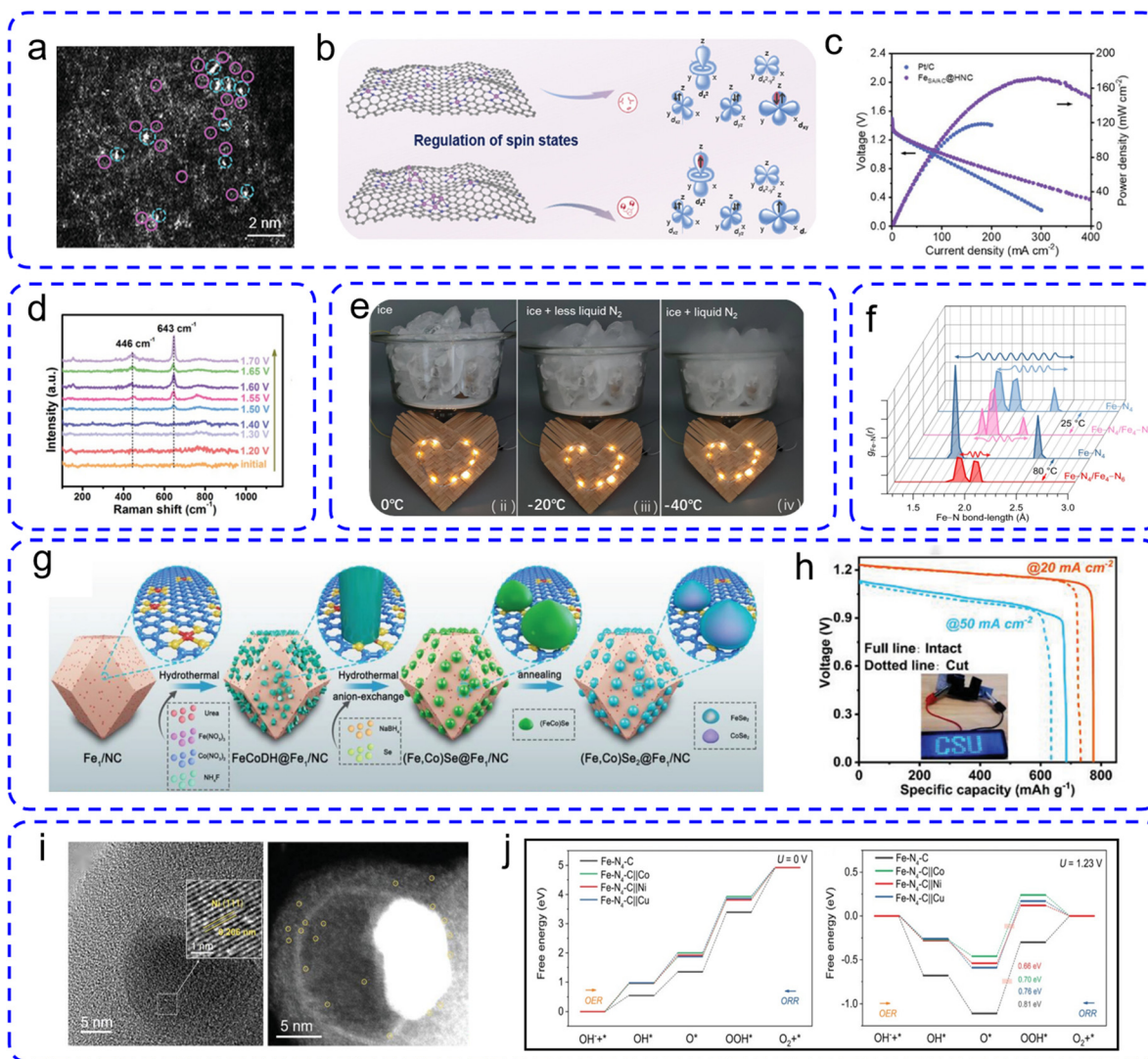
Fig. 11 (a) HAADF-STEM image and (b) schematic diagram of different spin states of Fe−N−C. (c) Discharge polarization curves and corresponding power density curves. Reproduced with permission.[188] Copyright 2024, Wiley-VCH. (d) *In situ* Raman spectra of Co-CoN$_4$@NCNs at different potentials for OER. Reproduced with permission.[185] Copyright 2022, Wiley-VCH. (e) Galvanostatic charging and discharging curves of R-ZAB. Reprinted with permission.[189] Copyright 2023, Elsevier B.V. (f) Fe−N radial distribution function profiles. Reprinted with permission.[190] Copyright 2022, Springer Nature. (g) Schematic illustration of synthetic strategy to (Fe,Co)Se$_2$@Fe$_1$/NC. (h) The specific capacity of ZABs assembled by (Fe,Co)Se$_2$@Fe$_1$/NC and those after cut. Reproduced with permission.[41] Copyright 2023, Wiley-VCH. (i) HAADF-STEM image of Fe−N@Ni-HCFs. Free energy diagrams of different intermediates on different models at (i) *U* = 0 V and (j) *U* = 1.23 V. Reproduced with permission.[191] Copyright 2022, Wiley-VCH.

demonstrated that the adjacent electron-rich Fe nanoclusters could significantly strengthen the anti-oxidation stability of the FeN$_4$ sites due to strong electron-transfer interactions.[189] The synthesized catalyst endowed a R-ZAB with ultralong stability of 2300 continuous cycles at a low temperature of −40 °C. As depicted in Fig. 11e, only two Zn//NCA/Fe$_{SA+NC}$ batteries in series were needed to light up 10 LEDs with a rated voltage of about 3.0 V at −40 °C, indicating great potential for practical applications. Another study also suggested that Fe clusters could alleviate demetallation *via* inhibiting the vibrations of Fe−N bonds on surrounding FeN$_4$ sites (Fig. 11f).[190] More interestingly, Rao *et al.* unveiled that the synergy effect between the Fe ACs and SAs not only reduced the spin-down

d-band center in the Fe SAs, but also efficiently suppressed Cl$^-$ adsorption on Fe SAs, thereby enhancing both the activity and stability of the catalyst in alkaline seawater-based ZABs.[80] This innovative design approach rooted in intricate seawater systems could inspire other energy technologies, contributing to the development of clean energy systems in a future fossil-fuel-free society.

Additionally, the electronic structures of single-atom metal sites could be effectively adjusted *via* the heterointerface between two hybrid components. The asymmetric structure, characterized by differing work functions on either side of the heterointerface, would generate an electric field to facilitate electron migration.[192−195] Lei's group successfully developed a

composite containing a heterointerface between atomic Fe–N–C and selenides ((Fe,Co)Se$_2$@Fe$_1$/NC) as a bifunctional oxygen catalyst with a low ΔE of 0.628 V (Fig. 11g).[41] The strong interfacial interaction between Fe single-atomic sites over substrates and (Fe,Co)Se$_2$ effectively accelerated the charge transfer and optimized the adsorption energy of intermediates. Remarkably, the R-ZABs rendered by (Fe,Co)Se$_2$@Fe$_1$/NC demonstrated exceptional resistance to mechanical damage, highlighting their considerable potential for secure energy storage under challenging conditions (Fig. 11h). It is a maverick approach for constructing a "core–shell" structure, featuring an external carbon shell with single-atom sites and internal nanoparticles for achieving bifunctional activity. Tian *et al.* designed and synthesized an advanced ORR/OER electrocatalyst (Fe–N@Ni-HCFs) where atomic Fe–N$_4$ moieties were supported on hollow carbon fibers with encapsulated Ni nanoparticles (Fig. 11i).[191] The special structure greatly hastened electron penetration from the inner Ni nanoparticles to the outer Fe–N–C layers, which induced electron distribution of the atomic Fe–N$_4$ sites to reduce reaction energy barriers toward ORR and OER (Fig. 11j). Nevertheless, achieving precise control over the "core–shell" configuration still faces considerable challenges. The diversity of guest groups enriches the selectivity of these strategies, positioning C-SACs as potentially more effective than most bifunctional catalysts. This ingenious design supplies a viable avenue for pursuing high-performance oxygen catalysts for R-ZABs.

5. Advanced C-SACs for oxygen electrocatalysis

The C-SACs have displayed tremendous prospects for application in bifunctional oxygen electrocatalysis due to their exceptional activity, selectivity, and durability. Although these C-SACs possess a similar M–N–C configuration with nitrogen coordination, those supported on different substrates do not always exhibit comparable catalytic efficiency.[100] This variation is understandable, as the metal centers' coordinated atoms might be nearly the same, yet the substrates can induce unique interactions between the metal and support. As listed in Table 1, researchers have exploited a series of ideal SACs anchored on various carbon substrates *via* combining the atomic-level modulation tactics. The section below will discuss

Table 1 Summary of bifunctional activity and R-ZAB performance of various C-SACs

Catalysts	Carbon base precursor	$E_{1/2}$	E_{10}	ΔE	Battery electrolyte	P_{max} (mW cm^{-2})	Cycling stability	Ref.
NCAG/Fe–Cu	Gelatin	0.94	1.61 1 M KOH	0.67	PANa/KOH-Zn^{2+}	186	800 cycles@5 mA cm^{-2}	71
FeCu-DSAs/NSC	Carboxymethyl chitosan	0.93	1.577 1 M KOH	0.647	Liquid KOH-Zn^{2+}	230.6	350 h@10 mA cm^{-2}	206
SA-Fe-SNC	Lignosulfonate	0.876	1.632	0.756	Liquid KOH-Zn^{2+}	218	200 h@5 mA cm^{-2}	207
NCA/Fe$_{SA+NC}$	Gelatin	0.92	1.57 1 M KOH	0.65	PAA/KOH-Zn^{2+}	236	1800 cycles@5 mA cm^{-2}	189
CoFe-FeNC	Tannic acid	0.876	1.526	0.65	Liquid KOH-Zn^{2+}	120.8	1200 h@10 mA cm^{-2}	187
CoN$_3$ NLF	Polyacryl-onitrile	0.863	1.54	0.668	Liquid KOH-Zn^{2+}	306	300 h@5 mA cm^{-2}	127
Fe–N@Ni-HCFs	Polyacryl-onitrile	0.88	1.567	0.687	PVA/KOH-Zn^{2+}	64.5	10 h@2 mA cm^{-2}	191
Co-N$_3$B-C	Melamine@L-alanine	0.867	1.595 1 M KOH	0.728	Liquid KOH-Zn^{2+}	253	110 h@5 mA cm^{-2}	72
Mo-O$_2$S$_2$-C tubes	Oleylamine	0.81	1.554 1 M KOH	0.744	Liquid KOH-Zn^{2+}	197	50 h@5 mA cm^{-2}	120
CoSA/NCs	Ammonium citrate	0.87	1.533 1 M KOH	0.663	PVA/KOH-Zn^{2+}	164.4	2000 cycles@2 mA cm^{-2}	114
Co$_H$ SA/NC	Urea formald-ehyde resin	0.874	1.63 1 M KOH	0.756	Liquid KOH-Zn^{2+}	191.7	250 h@5 mA cm^{-2}	208
Mn–N$_4$–C$_{12}$	ZIF-8	0.916	1.60	0.684	P(AA-*co*-AMPS)/LAP/KOH-Zn^{2+}	24.9 (−40 °C)	645 h (−40 °C)@2 mA cm^{-2}	29
CoN$_4$-NiN$_4$-C	ZIF-8	0.89	1.581	0.691	Liquid KOH-Zn^{2+}	155.9	340 cycles@2 mA cm^{-2}	169
FeCo-N$_3$O$_3$@C	Fe/ZIF-8	0.936	1.528	0.592	Liquid KOH-Zn^{2+}	143	240 h@10 mA cm^{-2}	184
FeN$_4$B-NiN$_4$B	Fe–Ni/ZIF-8	0.90	1.618	0.718	Liquid KOH-Zn^{2+}	236.9	1100 h@5 mA cm^{-2}	209
FeMn-DSAC	ZIF-8@ glucose@melamine	0.922	1.635	0.713	PAM/KOH-Zn^{2+}	184	80 h@2 mA cm^{-2}	179
CNT@SAC-Co/ NCP	CNT@ppy-ZIF-76	0.87	1.61	0.74	Liquid KOH-Zn^{2+}	172	40 h@5 mA cm^{-2}	186
Co-CoN$_4$@NCNs	PANI@RGO	0.83	1.54 1 M KOH	0.71	Liquid KOH-Zn^{2+}	131.6	1500 cycles@10 mA cm^{-2}	185
Co SA-NDGs	RGO@g-C$_3$N$_4$	0.87	1.58	0.71	PAM/KOH-Zn^{2+}	219.9	150 h@2 mA cm^{-2}	112
VMoON@NC	RGO@PDA	0.861	1.532	0.671	Liquid KOH-Zn^{2+}	376.4	630 h@10 mA cm^{-2}	200
FeMn–N/S–C	Aniline	0.924	1.617	0.693	Liquid KOH-Zn^{2+}	346	180 h (−40 °C)@2 mA cm^{-2}	210
Fe$_1$N$_4$O$_1$	ZIF-8@PDA	0.93	1.55	0.62	Liquid KOH-Zn^{2+}	306.1	315 h@10 mA cm^{-2}	40

ORR and OER were tested in 0.1 M KOH unless specified; all potentials (V) were converted to the RHE scale.

the structure–activity relationship in detail and summarize the most recent progress of four types of precursor-derived bifunctional C-SACs for sustainable R-ZABs.

5.1. Conventional carbon nanomaterial-suppoted SACs

5.1.1. Carbon nanotube-based SACs. One-dimension CNTs feature slender structures that can absorb/store electrons and also serve as electron transport channels.[196] Chen's group fabricated a catalyst consisting of Co single atoms and nanoparticles dispersed on N-doped carbon nanotubes (Co-NCNT).[197] The utilization of porous NCNT contributed to facilitating the electron transfer and exposing more active sites, thus enhancing the catalytic performance. Hence, the ZABs with Co-NCNT showed a high OCV of 1.61 V (Fig. 12a). It should be noted that the curvature of CNT-based catalysts can improve the catalytic performance. Hu *et al.* found that Sn-N$_4$ sites embedded in carbon nanotubes manifested better ORR/OER activity with a tiny ΔE of 0.60 V compared with that on flat graphene[198] because the suitable curvature caused by CNTs could alter the adsorption strengths of O intermediates on active sites (Fig. 12b and c).

5.1.2. Graphene-based SACs. Two-dimension graphene with a well-defined atomic structure and chemical environments is the most popular carbon substrate to prepare SACs.[199–202] Particularly, surface modifications through wet chemistry techniques are highly desirable due to their operability under mild conditions.[203] A recent theoretical study also suggested that N-coordination graphene is one of the promising supports for SACs by studying the ORR activities of a series of single-atom sites within the eight carbon-based substrates (Fig. 12d).[204] An innovative atomic Fe–N$_2$O$_2$ sites confined in graphene substrate could endow R-ZAB with a P_{max} of 164.7 mW cm^{-2} and a cycling stability of 150 h at 20 mA cm^{-2}.[201] Similar to CNTs, the graphene often shows obvious surface wrinkles which have been proved to effectively accelerate the reaction kinetics. For example, the curved atomic CoN$_4$ moieties supported on highly wrinkled nitrogen-doped graphene (Co SA-NDGs) showed an excellent bifunctional activity with a low ΔE of 0.71 V.[112] As shown in Fig. 12e and f, the quasi-solid-state Zn//Co SA-NDGs battery could stably operate at wide temperatures ranging from −40 to 60 °C. For the synthesis of graphene-based SACs, graphene oxides (GOs) have
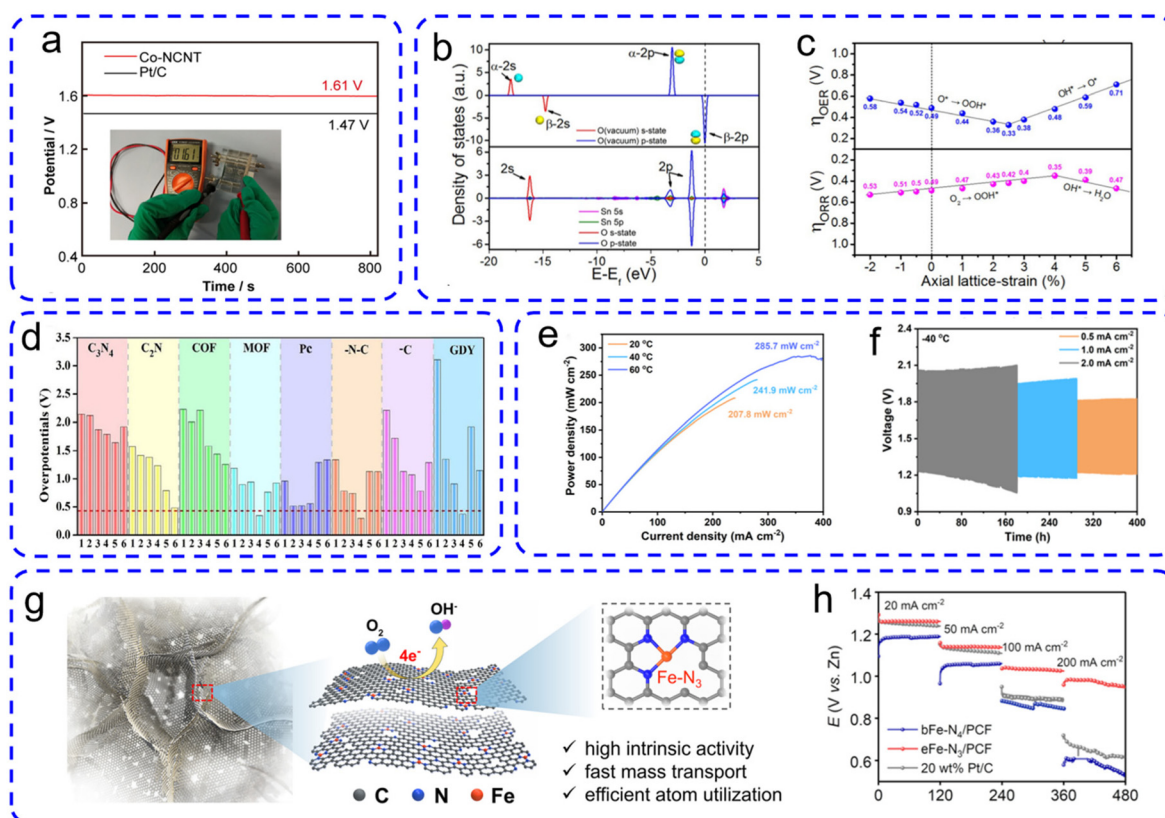

Fig. 12 (a) Voltage–time curves of Co-NCNT for ZAB. Reproduced with permission.[197] Copyright 2022, Springer Nature. (b) Density of states for the vacuum states of O* adsorbed on the Sn-N$_4$-CNT. (c) Relationships between calculated ORR/OER overpotentials and the axial lattice strain on Sn-N$_4$-CNT. Reproduced with permission.[198] Copyright 2023, American Chemical Society. (d) Summary of ORR overpotentials for TM atom doped different substrates. Reproduced with permission.[204] Copyright 2021, Springer Nature. (e) Corresponding power density curves of R-ZABs with Co SA-NDGs at different temperatures. (f) Charge/discharge curves of R-ZABs assembled by Co SA-NDGs at −40 °C. Reprinted with permission.[112] Copyright 2022, Springer Nature. (g) Schematic illustration of the designed advantageous features of eFe–N$_3$/PCF for ORR catalysis. (h) The discharge platforms of different catalysts at various current densities in ZABs. Reproduced with permission.[39] Copyright 2021, Elsevier B.V.

emerged as the most widely used precursors because their functional groups and defective sites can effectively immobilize metal single atoms.[199,205] Furthermore, the GO precursors can be thermally reduced and self-assembled into 3D graphene aerogels with abundant porous structure, promoting mass transfer. Liu *et al.* prepared a Fe–N/C catalyst including edge-hosted Fe–N$_3$ sites supported on 3D porous graphene frameworks which demonstrated high intrinsic activity and excellent mass-transport efficiency, thus in turn enabling high-rate capabilities at high current densities for R-ZABs (Fig. 12g and h).[39] Nevertheless, the reduction treatment of GO may result in irreversible restacking between individual graphene sheets. Therefore, it is crucial to pursue appropriate methods for preventing stacking during the preparation process of graphene-supported SACs.

5.2. MOF-derived C-SACs

Metal–organic frameworks (MOFs) are a type of emerging porous material which are composed of metal dots and organic moieties, characterized by large specific surface areas, well-defined structures and feasible functionalization.[211,212] The special features of MOFs can not only guarantee a uniform distribution of metal atoms supported within the carbon skeleton, but also generate rich microporous structures through the decomposition of organic linker or evaporation of certain metal atoms during carbonization.[213,214] Hence, MOFs have been considered as a type of prominent precursor for fabricating carbon-supported SACs.

Lately, as a representative MOF series, zeolitic imidazolate frameworks (ZIFs) have been widely reported. Particularly, ZIF-67 with a Co center and ZIF-8 with a Zn center have aroused extensive attention due to their easy synthesis route and flexible metal doping.[171,186] Benefiting from the porous characteristics of the original ZIF, a general host–guest strategy is commonly applied to fabricate metal single-atom-site catalysts.[152,211] The micropore channel of ZIF could serve as a molecular cage to isolate the metal species, thus partly suppressing the formation of large metal nanoparticles during pyrolysis. For example, ZIF-8 could capture $Mn_2(CO)_{10}$ precursors *in situ* during the crystallization process, due to the larger cavity diameter of the porous ZIF-8 host compared with the $Mn_2(CO)_{10}$ guest (Fig. 13a).[29] The generated edge-hosted Mn–N$_4$–C$_{12}$ coordination by subsequent pyrolysis showed a reversible ORR/OER electrocatalytic performance with a low ΔE of only 0.684 V for oxygen electrocatalysis and a good stability of 1800 cycles in ZABs (Fig. 13b and c). Moreover, the assembled solid-state ZABs could endure ultralow operating temperatures down to −40 °C and showed excellent energy efficiency. Using the ion exchange strategy, the preparation of bi- or even multi-metal doped carbon-based catalysts is easily achieved. Wang *et al.* constructed a Ni, Fe@ZIF-8 hybrid structure by replacing the position of Zn ions in ZIF-8 with Fe/Ni ions (Fig. 13d).[215] Then, the bifunctional catalysts derived from ZIF containing dual-metal atoms and nanoclusters were successfully obtained, displaying enhanced ORR/OER activities and a P_{max} of 217.5 mW cm^{-2} in ZABs, outperforming the performance of

Pt/C + RuO$_2$ (Fig. 13e and f). Two-step pyrolysis is an optimal route to prevent the collapse or deformation of the pore structure and frameworks. As shown in Fig. 13g, ZIF-8 was first exploited as a precursor to prepare the hierarchical N-doped porous carbon *via* carbonization.[216] Ferrocene subsequently vaporized and deposited on the hierarchical carbon derived from ZIF-8 to form Fe-SA@NC.

Changing the type of solution or metal ions used in the synthesis process can cause a shape change in the pre-prepared MOF. Unlike the typical formation of polyhedra in methanol solvent, Zn/Co bimetallic MOF transformed into an accordion-like structure in acetic acid solution, which could maximize the density of Co single-atomic sites and their accessibility.[218] Similarly, Yang *et al.* fabricated densely accessible FeN$_4$ sites embedded on ultrathin ZIF-derived carbon nanosheets (1.11 × 1020 sites per g), which endowed the ZABs with P_{max} of 306 mW cm^{-2} and superb stability over 180 h (Fig. 13h and i).[217] It is noteworthy that MOF-derived carbon contains numerous micropores, yet has a relatively low count of mesopores and macropores. Therefore, nanostructure design with appropriate pores within MOFs is a significant method to promote the mass transfer efficiency and site accessibility for enhancing ORR/OER activities.[213,219] Polyethylene balls are often used as pore-forming agents for synthesizing ZIF-derived C-SACs with a trimodal-porous structure configured by highly ordered macropores interconnected through mesopores.[171,220] Other MOF materials (*e.g.*, UiO-66, porphyrinic MOFs, MIL-101, *etc.*) have also been reported as precursors for synthesizing highly active C-SACs.[211] The outstanding electrochemical properties of MOF-derived C-SACs make them promising candidates for promoting the performances of R-ZABs.

5.3. Biomass-derived C-SACs

As green carbon feedstock, biomass materials have long been known for their renewable nature for sustainability, abundance for low cost, and high carbon content for advanced performance.[221] Especially, saccharide-containing functional molecules, aromatic compounds, protein, and biomass waste have been widely used to synthesize C-SACs.[206,222,223] Generally, the various oxygen functional groups (*e.g.*, –OH, –COOH, –NH$_2$) in biomass can coordinate with metal ions to form metal–biomass composites, which is critical for inhibiting metal agglomeration and facilitating the formation of single atom sites.[147,168,224] Their carbon chain will *in situ* transform into carbon skeletons during the pyrolysis process; the metal ions may meanwhile convert into single-atom sites strongly trapped by heteroatoms on a carbon substrate.

Typically, to modify carbon substrates with heteroatoms, additional sources of heteroatoms will be introduced into the precursor mixture through appropriate methods.[120,134,139] Nevertheless, S, N and O elements are the basic components of biomass materials, so heteroatom self-doping can be also achieved during the pyrolysis process. For instance, Zhou *et al.* synthesized oxygen-coordinated Ni single atoms with outstanding OER activity using only sucrose as a carbon/oxygen source.[225] Lignosulfonate was also applied as a multifunc-
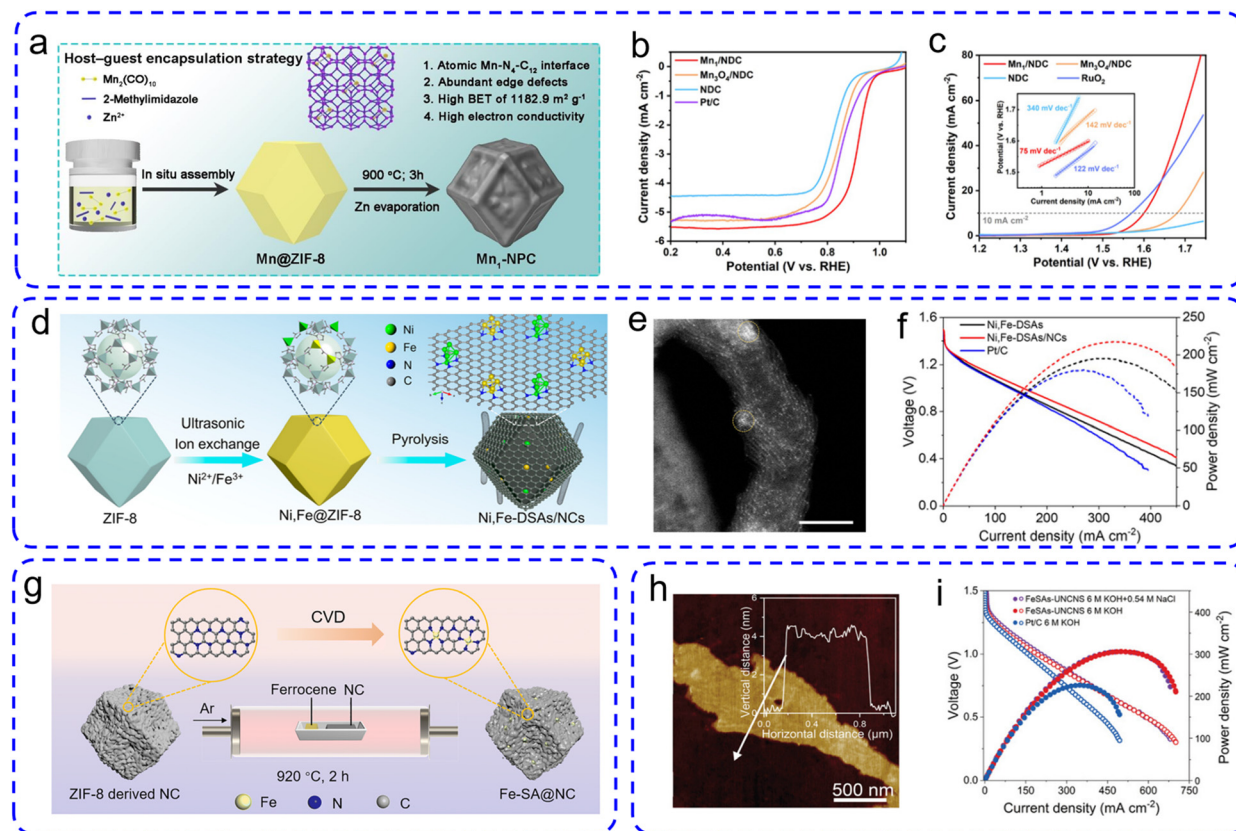
Fig. 13 (a) Scheme of the synthetic route of Mn_1-NPC. LSV curves of (b) ORR and (c) OER of four catalysts. Reproduced with permission.[29] Copyright 2023, American Chemical Society. (d) Schematics of the synthesis procedure and (e) HAADF-STEM images of Ni, Fe-DSAs/NCs. (f) Discharge polarization curves and corresponding power density curves. Reproduced with permission.[215] Copyright 2023, American Chemical Society. (g) Schematic illustration of the preparation of Fe-SA@NC. Reproduced with permission.[216] Copyright 2024, Royal Society of Chemistry. (h) The AFM image of FeSAs-UNCNS. (i) Polarization and power density curves of R-ZABs. Reproduced with permission.[217] Copyright 2023, Wiley-VCH.

tional bioligand for the fabrication of Fe–N_4–S SACs through strong metal-S/N coordination (Fig. 14a).[207] The negative charge distribution around Fe–N_4 sites induced the self-doping of S and accounted for its heightened ORR/OER performance (Fig. 14b). When tested in liquid ZABs, the Fe–N_4–S SACs cathode displayed a low ΔE of 0.75 V (Fig. 14c) and high specific capacity of 798.7 mA h g^{-1}. Employing diverse strategies to alter the physical and chemical characteristics of biomass-derived carbon can optimize their electrochemical performance. Certain hard templates could create unique pore structures and improve the density of metal sites in C-SACs.[26,189,224] Tang's groups synthesized a Co-based bifunctional electrocatalyst *via* direct solid-phase pyrolysis, utilizing $Co(NO_3)_2$ as the Co precursor, SiO_2 nanospheres as hard template and glucosamine as the N/C precursor.[226] As shown in Fig. 14d, the catalyst presented abundant spherical voids after the removal of SiO_2, which led to a porous N-modified carbon skeleton with atomically dispersed Co_2–N_6 binuclear sites.

Furthermore, biomass hydrogels are a type of promising precursor for the preparation of carbon aerogel-based SACs. The abundant nanowrinkles and microporous defects in carbon aerogels resulting from the tortuous and interlaced

hydrogel chain could not only capture and stabilize isolated metal atoms but also improved the intrinsic activity of the atomic sites.[71,147] He *et al.* prepared nanowrinkled carbon aerogels embedded with FeN_x single sites ($NCA_{C–Zn}$/Fe) by pyrolysis of chitosan-Zn hydrogel containing Fe complex and SiO_2 template (Fig. 14e).[224] The prepared $NCA_{C–Zn}$/Fe possessed excellent bifunctional electrocatalytic activity with ΔE of 0.71 V and greater power density than Pt/C-RuO_2 catalysts in aqueous R-ZABs. DFT calculation indicated that FeN_x sites in carbon nanowrinkles were most likely responsible for the enhanced reaction activity. Hydrogel precursors for designing advanced oxygen electrocatalysts based on atomically dispersed metal centers have also been reported, utilizing cellulose, starch, gelatin, and alginate.[26,222,228] Solid biomass waste-derived carbon materials often inherit the naturally well-interconnected nanochannels of precursors, which can capture metal atoms and accelerate mass transport.[229,230] Zhong and coworkers designed and synthesized single-atom FeN_4 sites supported on wood-derived porous carbon *via* a facile $FeCl_3$ pretreatment and pyrolysis process (Fig. 14f).[227] The two-step process could effectively generate rich microporous structures in the wood cell walls and successfully intro-
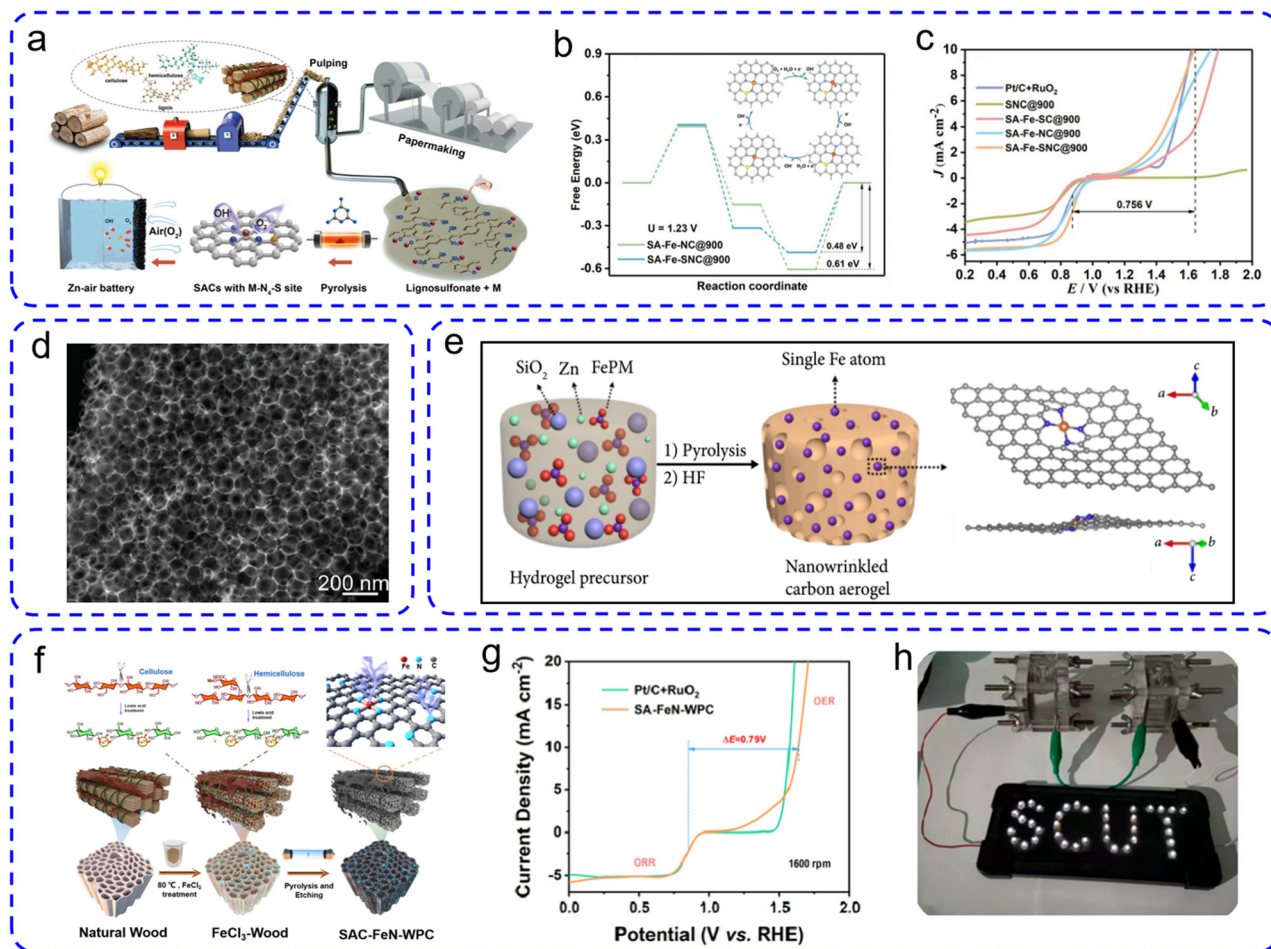
Fig. 14 (a) Illustration of fabrication of SACs with M–N$_4$–S sites from lignosulfonate. (b) Free energy diagram for SA-Fe-SNC@900 and SA-Fe-NC@900 during ORR. (c) Polarization curves for ORR and OER bifunctional catalytic activity. Reproduced with permission.[207] Copyright 2023, Wiley-VCH. (d) SEM images of Co$_2$-DAs@CHNSs. Reproduced with permission.[226] Copyright 2024, Wiley-VCH. (e) Schematic of the synthesis of NCA$_{C–Zn}$/Fe carbon aerogel. Reproduced with permission.[224] Copyright 2019 by the authors. (f) Schematic illustration of the fabrication of SAC-FeN-WPC. (g) Polarization curves of the catalysts for bifunctional activity. (h) Image of the LED powered by two liquid ZABs. Reproduced with permission.[227] Copyright 2021, American Chemical Society.

duced atomically dispersed Fe–N active species into the micro-channels. The as-prepared Fe–N–C catalyst displayed excellent ORR/OER electrocatalytic performances and a great potential for practical application in R-ZABs (Fig. 14g and h). The above research fully demonstrates the feasibility of biomass materials in the sustainable preparation of cost-effective C-SACs for advanced bifunctional oxygen electrocatalysis, which provides a promising strategy to achieve the valorization of underused biomass resource.

5.4. Small-molecule and polymer-derived C-SACs

While ordinary polymers are frequently used as precursors for directly synthesizing heteroatom-doped metal-free carbon catalysts, their oxygen electrocatalytic activity remains inferior to that of noble metal catalysts.[235] In recent years, metal–polymer hybrids with uniformly coordinated metal species have gained attention for fabricating sophisticated C-SACs.[208,236,237] In particular, resin with a cross-linked porous framework can coordi-

nate with various metal ions due to the abundance of –NH$_2$ or –OH groups present. For example, urea formaldehyde resin (UFR) with rich N content could produce an N-functionalized porous structure for anchoring more metal species during pyrolysis. Based on this, Xie *et al.* constructed high-density and accessible Co–N$_4$ sites on UFR-derived porous carbon (Co$_H$ SA/NC).[208] As depicted in Fig. 15a, the Co$_H$ SA/NC showed the form of carbon foam composed of stacked and interconnected 2D graphene-like nanosheets. DFT calculations revealed that the highly dense Co–N$_4$ sites could lead to a redistribution of the Co-d orbital, thus improving oxygen electrocatalytic activity (Fig. 15b). In turn, this Co$_H$ SA/NC electrode exhibited an excellent discharging performance with a P_{max} of 191.7 mW cm^{-2}.

As an emerging porous molecular framework, covalent organic frameworks (COFs) could be utilized to construct COF-derived C-SACs through simple absorption–pyrolysis methods. Chen *et al.* synthesized a Co–N–C single-atom catalyst
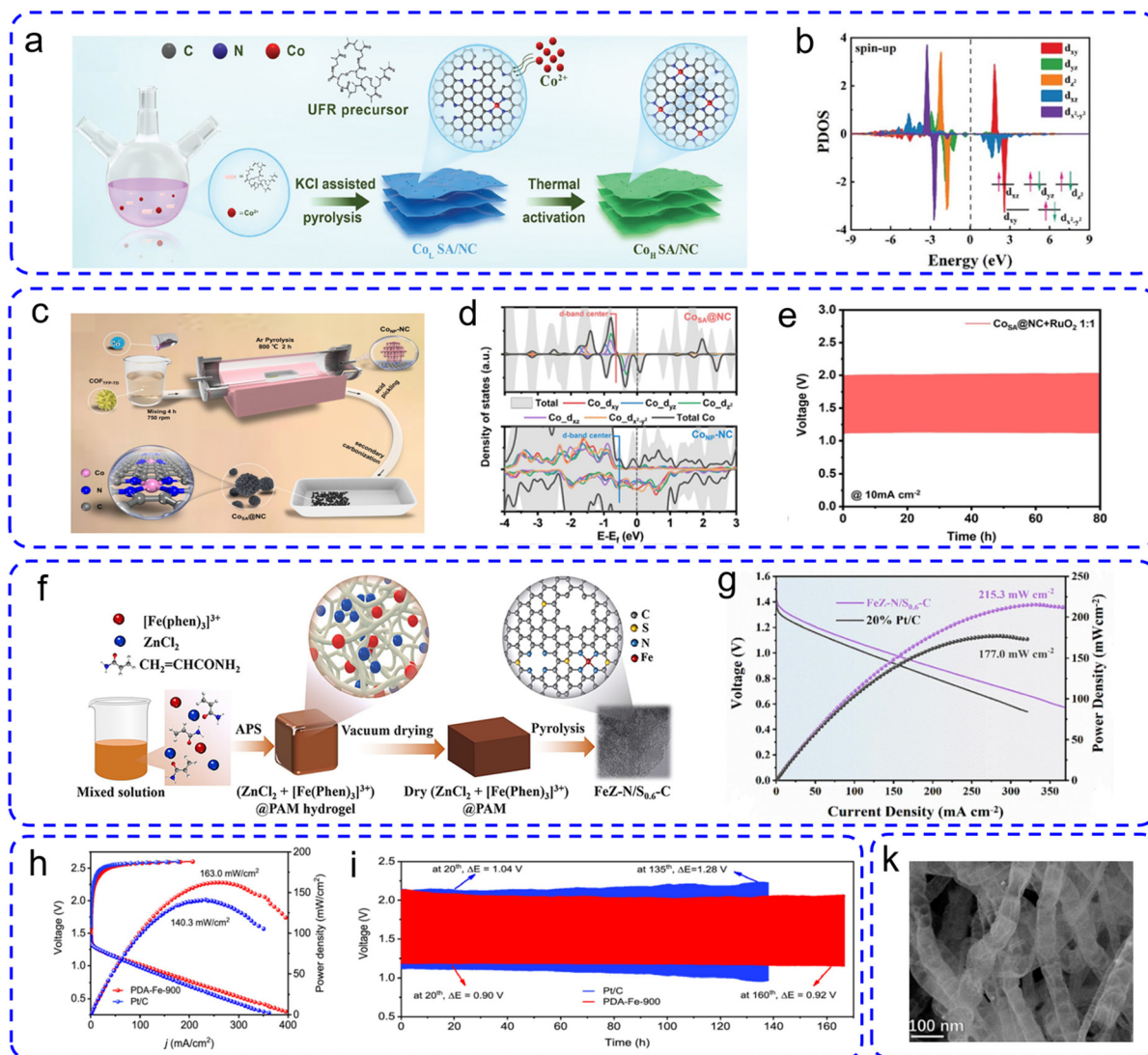
Fig. 15 (a) Schematic diagram of the preparation process of Co_H SA/NC. (b) The PDOS for Co-3d orbitals in H-CoN$_4$. Reproduced with permission.[208] Copyright 2024, Wiley-VCH. (c) The scheme diagram for preparing Co_{NP}-NC and Co_{SA}@NC. (d) Crystal orbitals Hamilton population (COHP) plots of Co_{SA}@NC. (e) Long-term rechargeable curves of the R-ZAB assembled by Co_{SA}@NC + RuO$_2$. Reproduced with permission.[231] Copyright 2024, Elsevier B.V. (f) Preparation of FeZ-N/S−C. (g) Discharge polarization curves and the corresponding power density curves of R-ZABs. Reproduced with permission.[232] Copyright 2024, Elsevier B.V. (h) Polarization and power density curves and (i) stability of the R-ZAB. Reproduced with permission.[233] Copyright 2023, Elsevier B.V. (j) Field emission scanning electron microscopy of Ni@NiNCNT. Reproduced with permission.[234] Copyright 2022, American Chemical Society.

(Co_{SA}@NC) using urchin-like COF$_{TFP-TD}$ assembled using terephthalic dihydrazide and 1,3,5-triformylphloroglucinol (Fig. 15c).[231] DFT calculations found that Co_{SA}@NC suggested a lower d-band center, thus accelerating the rate-determining step of the reaction (Fig. 15d). The Co_{SA}@NC-based ZAB demonstrated a high energy density of 896.5 W h kg^{-1} and discharging stability over 80 h at the current density of 10 mA cm^{-2} (Fig. 15e). In addition, monomers such as aniline, acrylamide, pyrrole, acrylic acid can polymerize with a crosslinking agent to form a polymer hydrogel, in which 3D porous nanostructures can provide a spatial confinement effect for the loading of metal precursors.[127,233,237] As shown in Fig. 15f, through one-step pyrolysis of polyacrylamide hydrogel contain-

ing [Fe(phen)$_3$]$^{3+}$ and ZnCl$_2$, nitrogen–sulfur co-doped catalyst (FeZ-N/S$_{0.6}$-C) with hierarchically porous structures and uniform FeN$_4$ active sites was fabricated.[232] FeZ-N/S$_{0.6}$-C as the air cathode endowed an aqueous ZAB with a high P_{max} of 215.3 mW cm^{-2} (Fig. 15g), and an excellent specific capacity of 816 m Ah g$_{Zn}^{-1}$. A recent study also suggested that the S, N co-doped carbonaceous nanosprings with Fe single atoms coupled with Fe$_3$C nanoparticles (FeNS/Fe$_3$C@CNS) could be achieved *via* the carbonization of twisted polypyrrole soft templates.[237] Theoretical and experimental findings indicated that the high curvature of twisted nanosprings and S substitution in the coordination layer could improve the oxygen electrocatalytic activity of atomically dispersed Fe sites for flexible R-ZABs.

Direct pyrolysis of the mixtures composed of small molecules and metal salts can also yield high-density metal single-atom sites. Zhang and coworkers fabricated dense and accessible Fe–N_x sites anchored on porous carbon fiber bundles *via* a ligand-assisted strategy using 2,6-diamino-pyridine (PDA) as C precursor, SBA-15 as hard templates, and 1,10-phenolline as space isolation agent.[233] As shown in Fig. 15h and i, the bifunctional activity of the as-synthesized PDA-Fe-900 was confirmed to possess a better discharging/charging performance for R-ZABs. It is interesting that nitrogen-containing small molecules can be converted into graphene sheets or carbon nanotubes during the high-temperature carbonization process.[209,238] For example, the Ni nanoparticle encapsulated by Ni- and N-codoped carbon nanotube (Ni@NiNCNT) was synthesized by pyrolyzing a mixture of Ni^{2+} and melamine.[234] As shown in Fig. 15k, a significant number of bamboo-like CNTs was generated through the catalytic growth from metallic species, resulting from the rearrangement of the carbonaceous gases decomposed from melamine during pyrolysis. As an air cathode catalyst for R-ZAB, the performance of Ni@NiNCNT exceeded that of Pt/C + RuO_2 mixture.

6. Conclusion and perspective

The initial batch of ZABs designed for bus commutes began trials in 2011. Each drive covered approximately 200 miles, with speeds reaching as high as 60 miles per hour.[239] At that time, the estimated cost of them was only 2/3 of that of LIBs. However, the system required the anode and electrolyte to be replaced after every drive, which increased both the costs and the manual labor involved. The US Department of Energy has established specific targets for fast-charging batteries used in electrified transportation by 2025 at the cell-pack level: over 300 W h kg^{-1}, \$75 per kW h, achieving 80% charge capacity in 15 min, and functioning effectively across a broad temperature range.[240] R-ZABs show significant potential to achieve these objectives and are regarded as a highly promising next-generation clean energy storage/conversion technology. Research by Santos *et al.* examined the costs associated with R-ZABs from various perspectives, including raw material supply, battery material production, manufacturing, and recycling.[241] They concluded that the cost of R-ZABs is linked to their cycle life and charge–discharge efficiency. With a cycle life of 1500 cycles, the power cost of the battery stands at \$2.3 k kW^{-1}, which is more economical than other existing battery technologies. At a cycle life of 2000 cycles, the capital cost reaches \$100 MW h per cycle, presenting a notable cost advantage. This value is higher than those reported for Li-ion or redox-flow batteries due to the current laboratory-scale production; there is room for improvement if an industrial scale fabrication is accomplished. The choice of catalyst plays a crucial role in battery performance, yet no catalyst currently combines excellent performance with low cost suitable for commercial R-ZABs applications. While zinc is relatively abundant, the necessity for precious metals in catalysts leads to a higher initial investment cost of R-ZABs, estimated at \$200 per kW h.

Recent advancements in oxygen electrocatalysts for R-ZABs have enhanced our understanding of these systems, particularly with the emergence of bifunctional C-SACs. These catalysts have revitalized the field owing to their low material cost, high atomic utilization efficiency and powerful activity. This comprehensive review primarily addresses the regulatory strategy for enhancing the oxygen electrocatalytic activity of C-SACs at the atomic level, including the modulation of the coordination environment of central metal atoms, heteroatom modification, defect engineering, geometric distortion effect, dual-metal site regulation, and guest groups strategy. It also explores the potential relationship between activity/stability and dynamic structure of active sites within C-SACs. Furthermore, recent progress in SACs anchored to four types of carbon substrate is summarized, covering design concepts and practical applications in high-performance R-ZABs. Although the development of bifunctional C-SACs has become increasingly mature, some challenges remain in their industrial application.

6.1. Upgrading the preparation methods

The cost competitiveness of catalyst preparation is crucial for commercialization. While carbon materials are considered inexpensive, the cost of functionalizing precursors and traditional high-temperature pyrolysis processes can undermine their cost efficiency in large-scale production. Moreover, regardless of whether bottom-up or top-down approaches are utilized, the prevention of metal agglomeration during synthesis is a critical issue.[242] Traditional high-temperature pyrolysis processes may also lead to the collapse of the pre-designed skeleton structure and the clumping of metal atoms, resulting in low loading (usually less than 1 wt%) of metal sites in targeted atomic catalysts. Simultaneously, some polluting chemicals, such as acids and bases for removing undesired metal species or templates, are also often used during the synthesis process. Strategies that involve more fabrication steps usually entail greater consideration and enhanced control, yielding a more uniform dispersion and increased metal loading.[243] However, the introduction of additional synthesis steps inherently raises complexity and results in higher material waste, ultimately diminishing yield. Hence, more efforts are needed in the development of efficient, green, advanced synthetic methodology to replace high energy consumption modes. Advancing large-scale (gram or kilogram) synthesis strategies is a vital focus in this area to facilitate the commercialization of C-SACs.[54] Presently, most prevalent techniques can only produce C-SACs at a milligram scale. Thus, simplifying the overall process—including precursors, steps, and equipment—is essential for achieving large-scale C-SAC synthesis.

6.2. Enhancing stability and OER activity

The stability of C-SACs, which is closely related to the lifespan of R-ZABs, is a crucial factor in assessing their suitability for large-scale production and industrial applications. Although C-SACs generally exhibit high storage stability due to the strong covalent bonds between central metal atoms and sur-

rounding substrate atoms, they may experience carbon corrosion and aggregation of active sites under operational conditions. For instance, Fe-based SACs have emerged as promising substitutes for Pt-based catalysts for ORR; however, their performance in ZABs tends to decline significantly over time. Specifically, carbon skeletons with poor crystallinity and abundant defects are prone to electrochemical oxidation and destruction of atomic metal sites at high potential (>0.9 V *vs.* RHE) during the charging process. Additionally, the insufficient OER activity (E_{10} generally greater than 1.55 V) of C-SACs results in high actual charging voltages for R-ZABs, exacerbating this issue.[244] While strategies to enhance stability—such as increasing the graphitization of carbon substrates and stabilizing metal active sites—have been proposed, the intrinsic drawbacks have yet to be fully addressed. Therefore, there is a pressing need to develop C-SACs with robust stability and superior OER activity. As is often the case in catalysis, achieving both high activity and stability is challenging, and this holds true for C-SACs as well. It is crucial to find a balance between activity and stability in catalyst design for industrial applications, and sometimes it is beneficial to compromise a certain level of activity to improve C-SAC stability. Notably, C-SACs demonstrate superior stability in acidic conditions compared with alkaline electrolytes. Acidic electrolytes are particularly significant as they help protect the air cathode from CO_2 poisoning. This advantage can be leveraged to develop innovative hybrid acid/alkali ZABs (AA-ZABs). A notable example is the hybrid AA-ZAB designed by Wen *et al.*, which successfully integrates efficient seawater desalination with high power density output.[245] Therefore, there is a need to create highly efficient and durable C-SACs specifically designed for ORR/OER in acidic environments, as well as to devise new battery architectures.

6.3. Exploring reaction mechanisms and active site structures

Despite noticeable differences in activity of the active sites, the reaction mechanism and intermediates involved in the oxygen electrocatalysis process are considered to be consistent. This uniformity is puzzling. Furthermore, the enhanced site density that arises from the incorporation of an additional metal can significantly influence the catalytic performance.[246] Nevertheless, accurately quantifying active sites using *in situ* electrochemical methods remains a challenging task.[210] The catalytic performance of the atomic catalysts is sensitive to coordination structure, local environment, and reaction conditions. Nevertheless, identifying the exact structure of C-SACs is challenging because most characterization methods only provide average structural information, failing to capture the diversity and non-uniformity within C-SACs. It is important to highlight that the catalyst surface is dynamic during reactions, often displaying a disordered arrangement due to the presence of various reactants, intermediates, and products, rather than an ordered crystalline structure. As a result, only a limited number of characterization techniques can effectively reveal the constantly changing configuration of C-SACs under practi-

cal operating conditions. Among these methods, XAS is particularly notable for its ability to offer insights into the dynamic structures of electrocatalysts without depending on long-range order. However, it is crucial to acknowledge that the spectroscopic features observed may not directly reflect the surface characteristics pertinent to the catalytic reactions, as XAS is a bulk-sensitive technique. Therefore, it is essential to utilize a variety of advanced characterization approaches, including *in situ/operando* techniques and time-resolved spectroscopy, to confirm the dynamic evolution of active sites and to elucidate the reaction mechanisms during the complex electrocatalytic processes. More importantly, a thorough understanding of the dynamic reaction mechanism could supply a general design principle to guide the structural adjustment of C-SACs, in turn replacing the trial-and-error method.

6.4. From laboratory study to practical application

The foregrounds of R-ZABs are destined to be promising and broad. In laboratory research, electrocatalysts are generally designed and tested under optimized conditions, such as with pure reactants, at room temperature, and in controlled humidity and air purity. To transition electrocatalysis to industrial applications, bifunctional oxygen electrocatalysts must be able to function effectively in more realistic environments, particularly under extreme conditions like those found in deep-sea, high-latitude, and space settings. For example, seawater-based ZABs are appealing due to the plentiful availability of seawater on Earth. However, operating in seawater introduces challenges related to ion interference and corrosion. In addition to focusing on bifunctional oxygen electrocatalysts for cathodes, attention should also be paid to ameliorating configurations of whole R-ZABs including anode and electrolyte. A primary challenge for the electrolyte when exposed to air is the loss of water and the risk of CO_2 poisoning. Current strategies to mitigate this issue mainly focus on improving the water retention and CO_2 resistance of the solid electrolyte through the introduction of hydrophilic groups, the creation of porous network structures, and the enhancement of viscosity.

In conclusion, we anticipate a crucial mission for C-SACs over the next decade, which involves translating significant laboratory-scale successes into industrial-level applications. This necessity drives researchers to establish higher standards in the design of C-SACs. Beyond material design, it is equally important to advance innovative characterization and simulation techniques, optimize entire R-ZAB systems, and explore practical environmental factors. These efforts are essential steps in advancing bifunctional C-SACs to the next level, ultimately paving the way for commercialization.

Author contributions

Yang Chen designed the framework of the review and wrote the review. Gan Wang looked up most of the papers and proposed some suggestions. Junhua Li provided the methodology

for the review. Ting He proposed adding or deleting contents in each section of the review. Yi Zhang, Heng Zhang, and You-Nian Liu conceived the project, supervised and discussed the review.

Data availability

All relevant data are within the paper.

Conflicts of interest

The authors declare no conflict of interest.

Acknowledgements

References

1 Z. W. Seh, J. Kibsgaard, C. F. Dickens, I. Chorkendorff, J. K. Nørskov and T. F. Jaramillo, *Science*, 2017, **355**, eaad4998.

2 J. Panidi, D. G. Georgiadou, T. Schoetz and T. Prodromakis, *Adv. Funct. Mater.*, 2022, **32**, 2200694.

3 M. Titirici, S. G. Baird, T. D. Sparks, S. M. Yang, A. Brandt-Talbot, O. Hosseinaei, D. P. Harper, R. M. Parker, S. Vignolini and L. A. Berglund, *JPhys Mater.*, 2022, **5**, 032001.

4 R. Girod, T. Lazaridis, H. A. Gasteiger and V. Tileli, *Nat. Catal.*, 2023, **6**, 383–391.

5 Y. Wang, Z. Wang, W. K. Pang, W. Lie, J. A. Yuwono, G. Liang, S. Liu, A. M. D. Angelo, J. Deng and Y. Fan, *Nat. Commun.*, 2023, **14**, 2720.

6 J. Xiao, F. Shi, T. Glossmann, C. Burnett and Z. Liu, *Nat. Energy*, 2023, **8**, 329–339.

7 Z. Li, L. P. Hou, N. Yao, X. Y. Li, Z. X. Chen, X. Chen, X. Q. Zhang, B. Q. Li and Q. Zhang, *Angew. Chem.*, 2023, **135**, e202309968.

8 W. Sun, F. Wang, B. Zhang, M. Zhang, V. Küpers, X. Ji, C. Theile, P. Bieker, K. Xu and C. Wang, *Science*, 2021, **371**, 46–51.

9 C. Pozo-Gonzalo and N. Ortiz-Vitoriano, *Curr. Opin. Electrochem.*, 2022, **36**, 101120.

10 L. Yue, D. Wang, Z. Wu, W. Zhao, Y. Ren, L. Zhang, B. Zhong, N. Li, B. Tang, Q. Liu, Y. Luo, A. M. Asiri, X. Guo and X. Sun, *Chem. Eng. J.*, 2022, **433**, 134477.

11 W. Zhao, X. Ma, L. Gao, X. Wang, Y. Luo, Y. Wang, T. Li, B. Ying, D. Zheng, S. Sun, Q. Liu, Y. Zheng, X. Sun and W. Feng, *Adv. Mater.*, 2024, **36**, 2305190.

12 W. Zhang, J. Zhang, N. Wang, K. Zhu, C. Yang, Y. Ai, F. Wang, Y. Tian, Y. Ma and Y. Ma, *Nat. Sci. Sustainable*, 2024, **7**, 463–473.

13 X.-W. Lv, Z. Wang, Z. Lai, Y. Liu, T. Ma, J. Geng and Z.-Y. Yuan, *Small*, 2024, **20**, 2306396.

14 Q. Wang, S. Kaushik, X. Xiao and Q. Xu, *Chem. Soc. Rev.*, 2023, **52**, 6139–6190.

15 J.-N. Liu, C.-X. Zhao, J. Wang, D. Ren, B.-Q. Li and Q. Zhang, *Energy Environ. Sci.*, 2022, **15**, 4542–4553.

16 J. Chen, J. Luo, Y. Xiang and Y. Yu, *J. Energy Chem.*, 2024, **91**, 178–193.

17 G. Nazir, A. Rehman, J.-H. Lee, C.-H. Kim, J. Gautam, K. Heo, S. Hussain, M. Ikram, A. A. AlObaid and S.-Y. Lee, *Nano-Micro Lett.*, 2024, **16**, 138.

18 X. Zou, M. Tang, Q. Lu, Y. Wang, Z. Shao and L. An, *Energy Environ. Sci.*, 2024, **17**, 386–424.

19 D. E. Ciurduc, C. de la Cruz, N. Patil, A. Mavrandonakis and R. Marcilla, *Energy Storage Mater.*, 2022, **53**, 532–543.

20 H.-F. Wang, C. Tang and Q. Zhang, *Adv. Funct. Mater.*, 2018, **28**, 1803329.

21 Y.-P. Deng, Y. Jiang, R. Liang, N. Chen, W. Chen, Z.-W. Yin, G. King, D. Su, X. Wang and Z. Chen, *J. Am. Chem. Soc.*, 2023, **145**, 20248–20260.

22 M. Xu, R. Cao, B. Hao, D. Wang, D. Luo, H. Dou and Z. Chen, *Angew. Chem.*, 2024, **136**, e202407380.

23 Y. Song, W. Li, K. Zhang, C. Han and A. Pan, *Adv. Energy Mater.*, 2024, **14**, 2303352.

24 J. Fu, R. Liang, G. Liu, A. Yu, Z. Bai, L. Yang and Z. Chen, *Adv. Mater.*, 2019, **31**, 1805230.

25 F. Gao, J. He, H. Wang, J. Lin, R. Chen, K. Yi, F. Huang, Z. Lin and M. Wang, *Nano Res. Energy*, 2022, **1**, 9120029.

26 Q. Li, Z. Sun, C. Yin, Y. Chen, D. Pan, B. Yu, Y. Zhang, T. He and S. Chen, *Chem. Eng. J.*, 2023, **458**, 141492.

27 H. Liu, F. Yu, K. Wu, G. Xu, C. Wu, H. K. Liu and S. X. Dou, *Small*, 2022, **18**, 2106635.

28 F. Dong, M. Wu, Z. Chen, X. Liu, G. Zhang, J. Qiao and S. Sun, *Nano-Micro Lett.*, 2022, **14**, 36.

29 Q. Wang, Y. Tan, S. Tang, W. Liu, Y. Zhang, X. Xiong and Y. Lei, *ACS Nano*, 2023, **17**, 9565–9574.

30 G. Chen, Y. Liu, S. Xue, R. Zhang, H. Lv, J. Zhang, L. Wu and R. Che, *Small*, 2024, **20**, 2308192.

31 A. Pendashteh, S. M. Vilela, I. Krivtsov, D. Ávila-Brande, J. Palma, P. Horcajada and R. Marcilla, *J. Power Sources*, 2019, **427**, 299–308.

32 D. U. Lee, J.-Y. Choi, K. Feng, H. W. Park and Z. Chen, *Adv. Energy Mater.*, 2014, **4**, 1301389.

33 X. Liu, M. Park, M. G. Kim, S. Gupta, X. Wang, G. Wu and J. Cho, *Nano Energy*, 2016, **20**, 315–325.

34 F. Meng, H. Zhong, D. Bao, J. Yan and X. Zhang, *J. Am. Chem. Soc.*, 2016, **138**, 10226–10231.

35 C. Tang, B. Wang, H.-F. Wang and Q. Zhang, *Adv. Mater.*, 2017, **29**, 1703185.

36 Y. Pan, S. Liu, K. Sun, X. Chen, B. Wang, K. Wu, X. Cao, W.-C. Cheong, R. Shen, A. Han, Z. Chen, L. Zheng, J. Luo, Y. Lin, Y. Liu, D. Wang, Q. Peng, Q. Zhang, C. Chen and Y. Li, *Angew. Chem., Int. Ed.*, 2018, **57**, 8614–8618.

37 W. Xie, Y. Song, S. Li, J. Li, Y. Yang, W. Liu, M. Shao and M. Wei, *Adv. Funct. Mater.*, 2019, **29**, 1906477.

38 H. Shang, W. Sun, R. Sui, J. Pei, L. Zheng, J. Dong, Z. Jiang, D. Zhou, Z. Zhuang, W. Chen, J. Zhang, D. Wang and Y. Li, *Nano Lett.*, 2020, **20**, 5443–5450.

39 J. Liu, Z. Gong, C. Allen, W. Ge, H. Gong, J. Liao, J. Liu, K. Huang, M. Yan and R. Liu, *Chem Catal.*, 2021, **1**, 1291–1307.

40 Z. Li, S. Ji, C. Xu, L. Leng, H. Liu, J. H. Horton, L. Du, J. Gao, C. He, X. Qi, Q. Xu and J. Zhu, *Adv. Mater.*, 2023, **35**, 2209644.

41 H. Zheng, S. Wang, S. Liu, J. Wu, J. Guan, Q. Li, Y. Wang, Y. Tao, S. Hu, Y. Bai, J. Wang, X. Xiong, Y. Xiong and Y. Lei, *Adv. Funct. Mater.*, 2023, **33**, 2300815.

42 Y. Li, A. Huang, L. Zhou, B. Li, M. Zheng, Z. Zhuang, C. Chen, C. Chen, F. Kang and R. Lv, *Nat. Commun.*, 2024, **15**, 8365.

43 Z. Chen, A. Yu, D. Higgins, H. Li, H. Wang and Z. Chen, *Nano Lett.*, 2012, **12**, 1946–1952.

44 H. Li, X. Shu, P. Tong, J. Zhang, P. An, Z. Lv, H. Tian, J. Zhang and H. Xia, *Small*, 2021, **17**, 2102002.

45 A. Pendashteh, J. Palma, M. Anderson and R. Marcilla, *Appl. Catal., B*, 2017, **201**, 241–252.

46 X. Tian, M. Xu, X. Ma, G. Mu, J. Xiao and S. Wang, *ChemSusChem*, 2024, **17**, e202400570.

47 X. Cao, Y. Yang, X. Yan, N. J. Geels, J.-L. Luo and N. Yan, *Green Chem.*, 2020, **22**, 6075–6083.

48 Q. An, S. Bo, J. Jiang, C. Gong, H. Su, W. Cheng and Q. Liu, *Adv. Sci.*, 2023, **10**, 2205031.

49 X. Wang, Z. Kang, D. Wang, Y. Zhao, X. Xiang, H. Shang and B. Zhang, *Nano Energy*, 2024, **121**, 109268.

50 W. Xue, Q. Zhou, X. Cui, J. Zhang, S. Zuo, F. Mo, J. Jiang, X. Zhu and Z. Lin, *Angew. Chem., Int. Ed.*, 2023, **62**, e202307504.

51 S. C. Sarma, J. Barrio, M. Gong, A. Pedersen, A. Kucernak, M. Titirici and I. E. Stephens, *Electrochim. Acta*, 2023, **463**, 142855.

52 J.-N. Liu, C.-X. Zhao, J. Wang, X.-Q. Fang, C.-X. Bi, B.-Q. Li and Q. Zhang, *Joule*, 2024, **8**, 1804–1819.

53 C. Ye, M. Zheng, Z. Li, Q. Fan, H. Ma, X. Fu, D. Wang, J. Wang and Y. Li, *Angew. Chem., Int. Ed.*, 2022, **61**, e202213366.

54 C. Jia, Q. Sun, R. Liu, G. Mao, T. Maschmeyer, J. J. Gooding, T. Zhang, L. Dai and C. Zhao, *Adv. Mater.*, 2024, **36**, 2404659.

55 Q. Wang, Y. Lei, Y. Wang, Y. Liu, C. Song, J. Zeng, Y. Song, X. Duan, D. Wang and Y. Li, *Energy Environ. Sci.*, 2020, **13**, 1593–1616.

56 X. Wang, Y. Zhang, J. Wu, Z. Zhang, Q. Liao, Z. Kang and Y. Zhang, *Chem. Rev.*, 2022, **122**, 1273–1348.

57 J. Schumann, M. Stamatakis, A. Michaelides and R. Réocreux, *Nat. Chem.*, 2024, **16**, 749–754.

58 J. Zhuang and D. Wang, *Mater. Today Catal.*, 2023, **2**, 100009.

59 Z. Fang, Y. Li, J. Li, C. Shu, L. Zhong, S. Lu, C. Mo, M. Yang and D. Yu, *Angew. Chem., Int. Ed.*, 2021, **60**, 17615–17621.

60 Y. Yang, Y. Yang, Z. Pei, K.-H. Wu, C. Tan, H. Wang, L. Wei, A. Mahmood, C. Yan, J. Dong, S. Zhao and Y. Chen, *Matter*, 2020, **3**, 1442–1476.

61 X. Qin, Z. Wang, J. Han, Y. Luo, F. Xie, G. Cui, X. Guo and X. Sun, *Chem. Commun.*, 2018, **54**, 7693–7696.

62 C.-X. Zhao, X. Liu, J.-N. Liu, J. Wang, X. Wan, X.-Y. Li, C. Tang, C. Wang, L. Song, J. Shui, H.-J. Peng, B.-Q. Li and Q. Zhang, *J. Am. Chem. Soc.*, 2023, **145**, 27531–27538.

63 J. Wang, C.-X. Zhao, J.-N. Liu, D. Ren, X. Ma, B.-Q. Li, J.-Q. Huang and Q. Zhang, *Particuology*, 2023, **77**, 146–152.

64 G. Zhang, F. Tang, X. Wang, L. Wang and Y.-N. Liu, *ACS Catal.*, 2022, **12**, 5786–5794.

65 Y. Shao, Z. Zha and H. Wang, *J. Energy Chem.*, 2021, **63**, 54–73.

66 Y. Chen, T. He, Y. Liu, Y. Liu, Y.-N. Liu, C. Liu and Y. Zhang, *Curr. Opin. Electrochem.*, 2023, **37**, 101206.

67 G. Chen, H. Zhong and X. Feng, *Chem. Sci.*, 2021, **12**, 15802–15820.

68 X. Li, H. Rong, J. Zhang, D. Wang and Y. Li, *Nano Res.*, 2020, **13**, 1842–1855.

69 S. Wang, X.-T. Min, B. Qiao, N. Yan and T. Zhang, *Chin. J. Catal.*, 2023, **52**, 1–13.

70 J. Wang, C. Liu, S. Li, Y. Li, Q. Zhang, Q. Peng, S. T. John and Z. Wu, *Chem. Eng. J.*, 2022, **428**, 132558.

71 T. He, Y. Chen, Q. Liu, B. Lu, X. Song, H. Liu, M. Liu, Y. N. Liu, Y. Zhang and X. Ouyang, *Angew. Chem.*, 2022, **134**, e202201007.

72 G. Guan, Y. Liu, F. Li, X. Shi, L. Liu, T. Wang, X. Xu, M. Zhao, J. Ding and H. B. Yang, *Adv. Funct. Mater.*, 2024, **34**, 2408111.

73 J. Shan, C. Ye, Y. Jiang, M. Jaroniec, Y. Zheng and S.-Z. Qiao, *Sci. Adv.*, 2022, **8**, eabo0762.

74 J. Wu, Y. Wang, D. Deng, Y. Bai, M. Liu, X. Zhao, X. Xiong and Y. Lei, *J. Mater. Chem. A*, 2022, **10**, 19304–19319.

75 W. He, X. Li, C. Tang, S. Zhou, X. Lu, W. Li, X. Li, X. Zeng, P. Dong, Y. Zhang and Q. Zhang, *ACS Nano*, 2023, **17**, 22227–22239.

76 J. Yu, B.-Q. Li, C.-X. Zhao and Q. Zhang, *Energy Environ. Sci.*, 2020, **13**, 3253–3268.

77 J. Yu, C.-X. Zhao, J.-N. Liu, B.-Q. Li, C. Tang and Q. Zhang, *Green Chem. Eng.*, 2020, **1**, 117–123.

78 B. Xu, J. Liang, X. Sun and X. Xiong, *Green Chem.*, 2023, **25**, 3767–3790.

79 Z. Cai, J. Liang, Z. Li, T. Yan, C. Yang, S. Sun, M. Yue, X. Liu, T. Xie, Y. Wang, T. Li, Y. Luo, D. Zheng, Q. Liu, J. Zhao, X. Sun and B. Tang, *Nat. Commun.*, 2024, **15**, 6624.

80 P. Rao, Y. Liu, X. Shi, Y. Yu, Y. Zhou, R. Li, Y. Liang, D. Wu, J. Li, X. Tian and Z. Miao, *Adv. Funct. Mater.*, 2024, **34**, 2407121.

81 S. Chen and C. Zhi, *Nat. Rev. Chem.*, 2024, **8**, 493–494.

82 W.-F. Wu, X. Yan and Y. Zhan, *Chem. Eng. J.*, 2023, **451**, 138608.

83 L. An, Z. Zhang, J. Feng, F. Lv, Y. Li, R. Wang, M. Lu, R. B. Gupta, P. Xi and S. Zhang, *J. Am. Chem. Soc.*, 2018, **140**, 17624–17631.

84 L. Xie, X. Li, B. Wang, J. Meng, H. Lei, W. Zhang and R. Cao, *Angew. Chem., Int. Ed.*, 2019, **58**, 18883–18887.

85 C.-X. Zhao, L. Yu, J.-N. Liu, J. Wang, N. Yao, X.-Y. Li, X. Chen, B.-Q. Li and Q. Zhang, *Angew. Chem., Int. Ed.*, 2022, **61**, e202208042.

86 Q. Nian, T. Sun, S. Liu, H. Du, X. Ren and Z. Tao, *Chem. Eng. J.*, 2021, **423**, 130253.

87 C.-X. Zhao, J.-N. Liu, N. Yao, J. Wang, D. Ren, X. Chen, B.-Q. Li and Q. Zhang, *Angew. Chem., Int. Ed.*, 2021, **60**, 15281–15285.

88 H. Huang, A. Huang, D. Liu, W. Han, C.-H. Kuo, H.-Y. Chen, L. Li, H. Pan and S. Peng, *Adv. Mater.*, 2023, **35**, 2303109.

89 Y. Wei, H. Xia, H. Lan, D. Xue, B. Zhao, Y. Yu, Y. Hu and J.-N. Zhang, *Adv. Energy Mater.*, 2024, **14**, 2303011.

90 C.-X. Zhao, J.-N. Liu, N. Yao, X. Zeng, A. Chen, P. Dong, Y. Zhang, X. Ma, C. Tang, B.-Q. Li and Q. Zhang, *Renewables*, 2023, **1**, 73–80.

91 S. Chen, T. Wang, L. Ma, B. Zhou, J. Wu, D. Zhu, Y. Y. Li, J. Fan and C. Zhi, *Chem*, 2023, **9**, 497–510.

92 C. Gu, X.-Q. Xie, Y. Liang, J. Li, H. Wang, K. Wang, J. Liu, M. Wang, Y. Zhang, M. Li, H. Kong and C.-S. Liu, *Energy Environ. Sci.*, 2021, **14**, 4451–4462.

93 Z. Pei, Z. Yuan, C. Wang, S. Zhao, J. Fei, L. Wei, J. Chen, C. Wang, R. Qi, Z. Liu and Y. Chen, *Angew. Chem., Int. Ed.*, 2020, **59**, 4793–4799.

94 X. Zhong, Z. Zheng, J. Xu, X. Xiao, C. Sun, M. Zhang, J. Ma, B. Xu, K. Yu, X. Zhang, H.-M. Cheng and G. Zhou, *Adv. Mater.*, 2023, **35**, 2209980.

95 D. Wang, Q. Li, Y. Zhao, H. Hong, H. Li, Z. Huang, G. Liang, Q. Yang and C. Zhi, *Adv. Energy Mater.*, 2022, **12**, 2102707.

96 C. Xie, W. Chen, Y. Wang, Y. Yang and S. Wang, *Chem. Soc. Rev.*, 2024, **53**, 10852–10877.

97 P. Zhang, K. Chen, J. Li, M. Wang, M. Li, Y. Liu and Y. Pan, *Adv. Mater.*, 2023, **35**, 2303243.

98 J. Yang, W. Liu, M. Xu, X. Liu, H. Qi, L. Zhang, X. Yang, S. Niu, D. Zhou and Y. Liu, *J. Am. Chem. Soc.*, 2021, **143**, 14530–14539.

99 G. Xing, M. Tong, P. Yu, L. Wang, G. Zhang, C. Tian and H. Fu, *Angew. Chem., Int. Ed.*, 2022, **61**, e202211098.

100 H.-Y. Tan, S.-C. Lin, J. Wang, J.-H. Chen, C.-J. Chang, C.-H. Hou, J.-J. Shyue, T.-R. Kuo and H. M. Chen, *J. Am. Chem. Soc.*, 2023, **145**, 27054–27066.

101 M. Tong, F. Sun, Y. Xie, Y. Wang, Y. Yang, C. Tian, L. Wang and H. Fu, *Angew. Chem., Int. Ed.*, 2021, **60**, 14005–14012.

102 X. Li, C.-S. Cao, S.-F. Hung, Y.-R. Lu, W. Cai, A. I. Rykov, S. Miao, S. Xi, H. Yang, Z. Hu, J. Wang, J. Zhao, E. E. Alp, W. Xu, T.-S. Chan, H. Chen, Q. Xiong, H. Xiao, Y. Huang, J. Li, T. Zhang and B. Liu, *Chem*, 2020, **6**, 3440–3454.

103 Y. Zhao, H.-C. Chen, X. Ma, J. Li, Q. Yuan, P. Zhang, M. Wang, J. Li, M. Li, S. Wang, H. Guo, R. Hu, K.-H. Tu, W. Zhu, X. Li, X. Yang and Y. Pan, *Adv. Mater.*, 2024, **36**, 2308243.

104 W. Zhou, H. Su, Y. Li, M. Liu, H. Zhang, X. Zhang, X. Sun, Y. Xu, Q. Liu and S. Wei, *ACS Energy Lett.*, 2021, **6**, 3359–3366.

105 H. Shang, Z. Jiang, D. Zhou, J. Pei, Y. Wang, J. Dong, X. Zheng, J. Zhang and W. Chen, *Chem. Sci.*, 2020, **11**, 5994–5999.

106 X. Han, T. Zhang, W. Chen, B. Dong, G. Meng, L. Zheng, C. Yang, X. Sun, Z. Zhuang, D. Wang, A. Han and J. Liu, *Adv. Energy Mater.*, 2021, **11**, 2002753.

107 M. Tong, F. Sun, G. Xing, C. Tian, L. Wang and H. Fu, *Angew. Chem., Int. Ed.*, 2023, **62**, e202314933.

108 M. Liu, J. Zhang, H. Su, Y. Jiang, W. Zhou, C. Yang, S. Bo, J. Pan and Q. Liu, *Nat. Commun.*, 2024, **15**, 1675.

109 J. Cai, X. Hao, Z. Bian, Y. Wu, C. Wei, X. Yin, B. Liu, M. Fang, Y. Lv, Y. Xie, Y. Fang and G. Wang, *Angew. Chem., Int. Ed.*, 2024, **63**, e202409079.

110 S. Lu, Z. Zhang, C. Cheng, B. Zhang and Y. Shi, *Angew. Chem., Int. Ed.*, 2024, DOI: 10.1002/anie.202413308.

111 J. Zhang, W. Liu, F. He, M. Song, X. Huang, T. Shen, J. Li, C. Zhang, J. Zhang and D. Wang, *Chem. Eng. J.*, 2022, **438**, 135619.

112 Q. Wang, Q. Feng, Y. Lei, S. Tang, L. Xu, Y. Xiong, G. Fang, Y. Wang, P. Yang, J. Liu, W. Liu and X. Xiong, *Nat. Commun.*, 2022, **13**, 3689.

113 J. Liu, Z. Gong, M. Yan, G. He, H. Gong, G. Ye and H. Fei, *Small*, 2022, **18**, 2103824.

114 P. Li, H. Wang, X. Tan, W. Hu, M. Huang, J. Shi, J. Chen, S. Liu, Z. Shi and Z. Li, *Appl. Catal., B*, 2022, **316**, 121674.

115 J. Liu, J. Xiao, B. Luo, E. Tian and G. I. N. Waterhouse, *Chem. Eng. J.*, 2022, **427**, 132038.

116 H. Fei, J. Dong, Y. Feng, C. S. Allen, C. Wan, B. Volosskiy, M. Li, Z. Zhao, Y. Wang and H. Sun, *Nat. Catal.*, 2018, **1**, 63–72.

117 Y. Zhao, X. F. Lu, G. Fan, D. Luan, X. Gu and X. W. Lou, *Angew. Chem., Int. Ed.*, 2022, **61**, e202212542.

118 X. Liu, G. Zhang, L. Wang and H. Fu, *Small*, 2021, **17**, 2006766.

119 S. Dyjak, B. J. Jankiewicz, S. Kaniecki and W. Kiciński, *Green Chem.*, 2024, **26**, 2985–3020.

120 Y. Zhao, Z. Zhang, L. Liu, Y. Wang, T. Wu, W. Qin, S. Liu, B. Jia, H. Wu and D. Zhang, *J. Am. Chem. Soc.*, 2022, **144**, 20571–20581.

121 H. Shang, X. Zhou, J. Dong, A. Li, X. Zhao, Q. Liu, Y. Lin, J. Pei, Z. Li and Z. Jiang, *Nat. Commun.*, 2020, **11**, 3049.

122 X. Wang, X. Zhou, C. Li, H. Yao, C. Zhang, J. Zhou, R. Xu, L. Chu, H. Wang, M. Gu, H. Jiang and M. Huang, *Adv. Mater.*, 2022, **34**, 2204021.

123 Y. Li, H. Sun, L. Ren, K. Sun, L. Gao, X. Jin, Q. Xu, W. Liu and X. Sun, *Angew. Chem., Int. Ed.*, 2024, **63**, e202405334.

124 Z. Qi, Y. Zhou, R. Guan, Y. Fu and J. B. Baek, *Adv. Mater.*, 2023, **35**, 2210575.

125 Y. Dai, B. Liu, Z. Zhang, P. Guo, C. Liu, Y. Zhang, L. Zhao and Z. Wang, *Adv. Mater.*, 2023, **35**, 2210757.

126 Z. Qiao, R. Jiang, H. Xu, D. Cao and X. C. Zeng, *Angew. Chem., Int. Ed.*, 2024, **63**, e202407812.

127 X. Liu, Z. Wang, J. Wang, T. Tang, C. Li, J. Yu, S. Zhang and C. Deng, *Energy Storage Mater.*, 2024, **65**, 103184.

128 L. Peng, J. Yang, Y. Yang, F. Qian, Q. Wang, D. Sun-Waterhouse, L. Shang, T. Zhang and G. I. Waterhouse, *Adv. Mater.*, 2022, **34**, 2202544.

129 L. Li, S. Huang, R. Cao, K. Yuan, C. Lu, B. Huang, X. Tang, T. Hu, X. Zhuang and Y. Chen, *Small*, 2022, **18**, 2105387.

130 X. Tan, J. Zhang, F. Cao, Y. Liu, H. Yang, Q. Zhou, X. Li, R. Wang, Z. Li, H. Hu, Q. Zhao and M. Wu, *Adv. Sci.*, 2024, **11**, 2306599.

131 X. Li, X. Wu, Y. Zhao, Y. Lin, J. Zhao, C. Wu, H. Liu, L. Shan, L. Yang and L. Song, *Adv. Mater.*, 2023, **35**, 2302467.

132 G. Xiao, R. Lu, J. Liu, X. Liao, Z. Wang and Y. Zhao, *Nano Res.*, 2022, **15**, 3073–3081.

133 H. Shen, E. Gracia-Espino, J. Ma, H. Tang, X. Mamat, T. Wagberg, G. Hu and S. Guo, *Nano Energy*, 2017, **35**, 9–16.

134 X. Xie, H. Peng, G. Ma, Z. Lei and Y. Xu, *Mater. Chem. Front.*, 2023, **7**, 2595–2619.

135 Y. Li, C. Chen, G. Zhang, H. Huang, Y. Ren, S. Zuo, Z. Wu, L. Zheng, Z. Lai, J. Zhang, M. Rueping, Y. Han and H. Zhang, *Angew. Chem., Int. Ed.*, 2024, DOI: **10.1002/anie.202411218**.

136 X. Yan, H. Liu, Y. Jia, L. Zhang, W. Xu, X. Wang, J. Chen, D. Yang and X. Yao, *Cell Rep. Phys. Sci.*, 2020, **1**, 100083.

137 L. Yang, X. Zhang, L. Yu, J. Hou, Z. Zhou and R. Lv, *Adv. Mater.*, 2022, **34**, 2105410.

138 Y. Zhao, Z. Shen, J. Huo, X. Cao, P. Ou, J. Qu, X. Nie, J. Zhang, M. Wu and G. Wang, *Angew. Chem., Int. Ed.*, 2023, **62**, e202308349.

139 S. Li, J. Zhang, Y. Li, P. Fan and M. Wu, *Nano Res. Energy*, 2024, **3**, e9120098.

140 Y. Chen, Q. Sun, Z. Ni, X. Tu, C. Sun, S. Zhu, X. Duan, M. Jiang, Z. Xie and M. Liu, *Chem. Eng. J.*, 2024, **482**, 148853.

141 Y. Lin, K. Liu, K. Chen, Y. Xu, H. Li, J. Hu, Y.-R. Lu, T.-S. Chan, X. Qiu and J. Fu, *ACS Catal.*, 2021, **11**, 6304–6315.

142 Y. Jia and X. Yao, *Acc. Chem. Res.*, 2023, **56**, 948–958.

143 J. Zhu and S. Mu, *Adv. Funct. Mater.*, 2020, **30**, 2001097.

144 S. Jiang, G. Ye, W. Zhu, S. Liu, Z. He and G. Jin, *ACS Sustainable Chem. Eng.*, 2023, **11**, 16926–16934.

145 L. Lyu, X. Hu, S. Lee, W. Fan, G. Kim, J. Zhang, Z. Zhou and Y.-M. Kang, *J. Am. Chem. Soc.*, 2024, **146**, 4803–4813.

146 Q. Ye, X. Yi, C. Z. Wang, T. Zhang, Y. Liu, S. Lin and H. J. Fan, *Adv. Funct. Mater.*, 2024, **34**, 2400107.

147 T. He, Y. Song, Y. Chen, X. Song, B. Lu, Q. Liu, H. Liu, Y. Zhang, X. Ouyang and S. Chen, *Chem. Eng. J.*, 2022, **442**, 136337.

148 R. Gan, Y. Wang, X. Zhang, Y. Song, J. Shi and C. Ma, *J. Energy Chem.*, 2023, **83**, 602–611.

149 H. Tu, H. Zhang, Y. Song, P. Liu, Y. Hou, B. Xu, T. Liao, J. Guo and Z. Sun, *Adv. Sci.*, 2023, **10**, 2305194.

150 H. Tian, A. Song, P. Zhang, K. Sun, J. Wang, B. Sun, Q. Fan, G. Shao, C. Chen and H. Liu, *Adv. Mater.*, 2023, **35**, 2210714.

151 K. Khan, X. Yan, Q. Yu, S.-H. Bae, J. J. White, J. Liu, T. Liu, C. Sun, J. Kim and H.-M. Cheng, *Nano Energy*, 2021, **90**, 106488.

152 Q. Liang, W. Li, L. Xie, Y. He, B. Qiu, H. Zeng, S. Zhou, J. Zeng, T. Liu and M. Yan, *Nano Lett.*, 2022, **22**, 2889–2897.

153 T. He, Y. Zhang, Y. Chen, Z. Zhang, H. Wang, Y. Hu, M. Liu, C.-W. Pao, J.-L. Chen and L. Y. Chang, *J. Mater. Chem. A*, 2019, **7**, 20840–20846.

154 X. Zou, M. Tang, Q. Lu, Y. Wang, Z. Shao and L. An, *Energy Environ. Sci.*, 2023, **17**, 386–424.

155 C. Tang and Q. Zhang, *Adv. Mater.*, 2017, **29**, 1604103.

156 H. Xia, R. Pang, X. Dong, Q. Liu, J. Chen, E. Wang and J. Li, *J. Am. Chem. Soc.*, 2023, **145**, 25695–25704.

157 J. Zhu, Y. Huang, W. Mei, C. Zhao, C. Zhang, J. Zhang, I. S. Amiinu and S. Mu, *Angew. Chem., Int. Ed.*, 2019, **58**, 3859–3864.

158 Y. Wang, K. Liu, K. Li, X. Yang, J. Hu, T.-S. Chan, X. Qiu, W. Li and M. Liu, *Chem. Eng. J.*, 2022, **429**, 132119.

159 Y. Tan, Z. Zhang, S. Chen, W. Wu, L. Yu, R. Chen, F. Guo, Z. Wang and N. Cheng, *Adv. Funct. Mater.*, 2024, **34**, 2311337.

160 G. Han, X. Zhang, W. Liu, Q. Zhang, Z. Wang, J. Cheng, T. Yao, L. Gu, C. Du and Y. Gao, *Nat. Commun.*, 2021, **12**, 6335.

161 G. Chen, R. Lu, C. Li, J. Yu, X. Li, L. Ni, Q. Zhang, G. Zhu, S. Liu and J. Zhang, *Adv. Mater.*, 2023, **35**, 2300907.

162 Y. Zhu, Y. Jiang, H. Li, D. Zhang, L. Tao, X. Z. Fu, M. Liu and S. Wang, *Angew. Chem.*, 2024, **136**, e202319370.

163 Y. Kang, Y.-F. Li and Z.-P. Liu, *J. Phys. Chem. C*, 2024, **128**, 3127–3135.

164 P. Liu, B. Chen, C. Liang, W. Yao, Y. Cui, S. Hu, P. Zou, H. Zhang, H. J. Fan and C. Yang, *Adv. Mater.*, 2021, **33**, 2007377.

165 Y. Zhou, Y. Liang, J. Fu, K. Liu, Q. Chen, X. Wang, H. Li, L. Zhu, J. Hu and H. Pan, *Nano Lett.*, 2022, **22**, 1963–1970.

166 X. Zhang, S. Zhu, Y. Xu and Y. Wang, *J. Mater. Chem. A*, 2023, **11**, 23270–23277.

167 Y. Zheng, D.-S. Yang, J. M. Kweun, C. Li, K. Tan, F. Kong, C. Liang, Y. J. Chabal, Y. Y. Kim and M. Cho, *Nano Energy*, 2016, **30**, 443–449.

168 Y. Chen, S. Hu, F. Nichols, F. Bridges, S. Kan, T. He, Y. Zhang and S. Chen, *J. Mater. Chem. A*, 2020, **8**, 11649–11655.

169 Y. Yang, B. Li, Y. Liang, W. Ni, X. Li, G. Shen, L. Xu, Z. Chen, C. Zhu and J. X. Liang, *Adv. Sci.*, 2024, **11**, 2310231.

170 J. Chen, H. Li, C. Fan, Q. Meng, Y. Tang, X. Qiu, G. Fu and T. Ma, *Adv. Mater.*, 2020, **32**, 2003134.

171 Z. Zhu, H. Yin, Y. Wang, C. H. Chuang, L. Xing, M. Dong, Y. R. Lu, G. Casillas-Garcia, Y. Zheng and S. Chen, *Adv. Mater.*, 2020, **32**, 2004670.

172 Y. Li, W. Shan, M. J. Zachman, M. Wang, S. Hwang, H. Tabassum, J. Yang, X. Yang, S. Karakalos and Z. Feng, *Angew. Chem.*, 2022, **134**, e202205632.

173 L. Ran, Y. Xu, X. Zhu, S. Chen and X. Qiu, *ACS Nano*, 2023, **18**, 750–760.

174 Y. Zhou, Y. Liu, Z. Wang, C. Li, Z. Wang, S. Zhang and C. Deng, *Energy Storage Mater.*, 2023, **59**, 102772.

175 Z. Li, S. Ji, C. Wang, H. Liu, L. Leng, L. Du, J. Gao, M. Qiao, J. H. Horton and Y. Wang, *Adv. Mater.*, 2023, **35**, 2300905.

176 T. Liu, Y. Chen, A. Xu, X. Liu, D. Liu, S. Li, H. Huang, L. Xu, S. Jiang and Q. Luo, *Sci. China: Chem.*, 2024, **67**, 1352–1359.

177 Z. Jin, P. Li, Y. Meng, Z. Fang, D. Xiao and G. Yu, *Nat. Catal.*, 2021, **4**, 615–622.

178 W. Wan, Y. Zhao, S. Wei, C. A. Triana, J. Li, A. Arcifa, C. S. Allen, R. Cao and G. R. Patzke, *Nat. Commun.*, 2021, **12**, 5589.

179 T. Cui, Y. P. Wang, T. Ye, J. Wu, Z. Chen, J. Li, Y. Lei, D. Wang and Y. Li, *Angew. Chem., Int. Ed.*, 2022, **61**, e202115219.

180 J. Qiao, Y. You, L. Kong, W. Feng, H. Zhang, H. Huang, C. Li, W. He and Z. Sun, *Adv. Mater.*, 2024, **36**, 2405533.

181 C. Hu, G. Xing, W. Han, Y. Hao, C. Zhang, Y. Zhang, C. H. Kuo, H. Y. Chen, F. Hu and L. Li, *Adv. Mater.*, 2024, **36**, 2405763.

182 H. Li, J. Wang, R. Qi, Y. Hu, J. Zhang, H. Zhao, J. Zhang and Y. Zhao, *Appl. Catal., B*, 2021, **285**, 119778.

183 Y. He, X. Yang, Y. Li, L. Liu, S. Guo, C. Shu, F. Liu, Y. Liu, Q. Tan and G. Wu, *ACS Catal.*, 2022, **12**, 1216–1227.

184 B. Tang, Y. Zhou, Q. Ji, Z. Zhuang, L. Zhang, C. Wang, H. Hu, H. Wang, B. Mei and F. Song, *Nat. Synth.*, 2024, **3**, 878–890.

185 K. Ding, J. Hu, J. Luo, L. Zhao, W. Jin, Y. Liu, Z. Wu, G. Zou, H. Hou and X. Ji, *Adv. Funct. Mater.*, 2022, **32**, 2207331.

186 J. C. Li, Y. Meng, L. Zhang, G. Li, Z. Shi, P. X. Hou, C. Liu, H. M. Cheng and M. Shao, *Adv. Funct. Mater.*, 2021, **31**, 2103360.

187 S. Zhang, J. Yang, L. Yang, T. Yang, Y. Liu, L. Zhou, Z. Xu, X. Zhou and J. Tang, *Appl. Catal., B*, 2024, **359**, 124485.

188 H. Zhang, H. C. Chen, S. Feizpoor, L. Li, X. Zhang, X. Xu, Z. Zhuang, Z. Li, W. Hu and R. Snyders, *Adv. Mater.*, 2024, **36**, 2400523.

189 Y. Chen, T. He, Q. Liu, Y. Hu, H. Gu, L. Deng, H. Liu, Y. Liu, Y.-N. Liu and Y. Zhang, *Appl. Catal., B*, 2023, **323**, 122163.

190 X. Wan, Q. Liu, J. Liu, S. Liu, X. Liu, L. Zheng, J. Shang, R. Yu and J. Shui, *Nat. Commun.*, 2022, **13**, 2963.

191 Y. Tian, Z. Wu, M. Li, Q. Sun, H. Chen, D. Yuan, D. Deng, B. Johannessen, Y. Wang and Y. Zhong, *Adv. Funct. Mater.*, 2022, **32**, 2209273.

192 C. He, Q. Liu, H. Wang, C. Xia, F. M. Li, W. Guo and B. Y. Xia, *Small*, 2023, **19**, 2207474.

193 L. Zeng, Z. Zhao, Q. Huang, C. Zhou, W. Chen, K. Wang, M. Li, F. Lin, H. Luo and Y. Gu, *J. Am. Chem. Soc.*, 2023, **145**, 21432–21441.

194 Z. Jiang, S. Song, X. Zheng, X. Liang, Z. Li, H. Gu, Z. Li, Y. Wang, S. Liu and W. Chen, *J. Am. Chem. Soc.*, 2022, **144**, 19619–19626.

195 L. Wang, X. Hu, H. Li, Z. Huang, J. Huang, T. T. Isimjan and X. Yang, *Green Chem.*, 2024, **26**, 2011–2020.

196 W. Zhao, V. D. Trung, H. Li, J. Natsuki, J. Tan, W. Yang and T. Natsuki, *Chem. Eng. J.*, 2024, **494**, 153101.

197 J.-J. Chen, S. Gu, R. Hao, Z.-Y. Wang, M.-Q. Li, Z.-Q. Li, K. Liu, K.-M. Liao, Z.-Q. Wang and H. Huang, *Rare Met.*, 2022, **41**, 2055–2062.

198 H. Hu, P. Zhang, B.-B. Xiao and J.-L. Mi, *ACS Appl. Mater. Interfaces*, 2023, **15**, 23170–23184.

199 H. Gong, Z. Gong, J. Liu, G. Ye and H. Fei, *Adv. Funct. Mater.*, 2024, **34**, 2316438.

200 J. Balamurugan, P. M. Austeria, J. B. Kim, E. S. Jeong, H. H. Huang, D. H. Kim, N. Koratkar and S. O. Kim, *Adv. Mater.*, 2023, **35**, 2302625.

201 Y. Li, Y. Ding, B. Zhang, Y. Huang, H. Qi, P. Das, L. Zhang, X. Wang, Z.-S. Wu and X. Bao, *Energy Environ. Sci.*, 2023, **16**, 2629–2636.

202 Y. Liu, S. Zhang, C. Jiao, H. Chen, G. Wang, W. Wu, Z. Zhuo and J. Mao, *Adv. Sci.*, 2023, **10**, 2206107.

203 R. Saini, F. Naaz, A. H. Bashal, A. H. Pandit and U. Farooq, *Green Chem.*, 2024, **26**, 57–102.

204 Y. Wang, R. Hu, Y. Li, F. Wang, J. Shang and J. Shui, *Nano Res.*, 2022, **15**, 1054–1060.

205 H. Hu, Y. Meng, Y. Mei, P. X. Hou, C. Liu, H. M. Cheng, M. Shao and J. C. Li, *Energy Storage Mater.*, 2023, **54**, 517–523.

206 J. Peng, B. Hu, Z. Li, X. Zhong, J. Shi, S. Cui, X. Wang and B. Xu, *Energy Storage Mater.*, 2024, **68**, 103342.

207 Z. Chen, X. Peng, Z. Chen, T. Li, R. Zou, G. Shi, Y. Huang, P. Cui, J. Yu and Y. Chen, *Adv. Mater.*, 2023, **35**, 2209948.

208 X. Xie, H. Peng, K. Sun, W. Li, A. Liang, G. Ma, Z. Lei and Y. Xu, *Adv. Funct. Mater.*, 2024, **34**, 2316037.

209 Z. Wang, R. Xu, Q. Ye, X. Jin, Z. Lu, Z. Yang, Y. Wang, T. Yan, Y. Liu and Z. Pan, *Adv. Funct. Mater.*, 2024, **34**, 2315376.

210 Y. He, H. Li, Y. Wang, Y. Jia, Y. Liu and Q. Tan, *J. Energy Chem.*, 2024, **90**, 610–620.

211 W. Wang, D. Chen, F. Li, X. Xiao and Q. Xu, *Chem*, 2024, **10**, 86–133.

212 J. W. Maina, C. Pozo-Gonzalo, L. Kong, J. Schütz, M. Hill and L. F. Dumée, *Mater. Horiz.*, 2017, **4**, 345–361.

213 Y.-F. Guo, S. Zhao, N. Zhang, Z. Liu, P.-F. Wang, J. Zhang, Y. Xie and T.-F. Yi, *Energy Environ. Sci.*, 2024, **17**, 1725–1755.

214 P. Wei, H. Xie, X. Zhu, R. Zhao, L. Ji, X. Tong, Y. Luo, G. Cui, Z. Wang and X. Sun, *ACS Sustainable Chem. Eng.*, 2020, **8**, 29–33.

215 Z. Wang, X. Jin, R. Xu, Z. Yang, S. Ma, T. Yan, C. Zhu, J. Fang, Y. Liu and S.-J. Hwang, *ACS Nano*, 2023, **17**, 8622–8633.

216 J.-F. Gu, J. Wang, Q. Wu, C. Wang, F. Verpoort and S. Chaemchuen, *J. Mater. Chem. A*, 2024, **12**, 16528–16536.

217 X. Yang, B. Zhu, Z. Gao, C. Yang, J. Zhou, A. Han and J. Liu, *Adv. Sci.*, 2023, **11**, 2306594.

218 J. Gao, Y. Hu, Y. Wang, X. Lin, K. Hu, X. Lin, G. Xie, X. Liu, K. M. Reddy and Q. Yuan, *Small*, 2021, **17**, 2104684.

219 L. Zong, K. Fan, L. Cui, F. Lu, P. Liu, B. Li, S. Feng and L. Wang, *Angew. Chem.*, 2023, **135**, e202309784.

220 Z. Wang, Z. Lu, Q. Ye, Z. Yang, R. Xu, K. Kong, Y. Zhang, T. Yan, Y. Liu and Z. Pan, *Adv. Funct. Mater.*, 2024, **34**, 2315150.

221 X. Zhuang, H. Liang, X. Hu, S. Li, X. Zhang, Q. Zhang and L. Ma, *Green Chem.*, 2024, **26**, 9005–9024.

222 J. Li, G. Wang, W. Sui, A. M. Parvez, T. Xu, C. Si and J. Hu, *Adv. Colloid Interface Sci.*, 2024, **329**, 103176.

223 Y. Cao, Y. Sun, R. Zheng, Q. Wang, X. Li, H. Wei, L. Wang, Z. Li, F. Wang and N. Han, *Biomass Bioenergy*, 2023, **168**, 106676.

224 T. He, B. Lu, Y. Chen, Y. Wang, Y. Zhang, J. L. Davenport, A. P. Chen, C.-W. Pao, M. Liu and Z. Sun, *Research*, 2019, **2019**, 6813585.

225 Z.-H. Zhou, W.-H. Li, Z. Zhang, Q.-S. Huang, X.-C. Zhao and W. Cao, *ACS Appl. Mater. Interfaces*, 2022, **14**, 47542–47548.

226 T. Lu, Q. Zhou, J. Li, T. Li, J. Gong, S. Zhang, H. Pang, S. Xi, L. Xu, G. Luo, D. Sun, K. Sun and Y. Tang, *Adv. Funct. Mater.*, 2024, **34**, 2405564.

227 L. Zhong, C. Jiang, M. Zheng, X. Peng, T. Liu, S. Xi, X. Chi, Q. Zhang, L. Gu and S. Zhang, *ACS Energy Lett.*, 2021, **6**, 3624–3633.

228 M. Shen, W. Hu, C. Duan, J. Li, S. Ding, L. Zhang, J. Zhu and Y. Ni, *J. Colloid Interface Sci.*, 2023, **629**, 778–785.

229 J. Chen, C. Qiu, L. Zhang, B. Wang, P. Zhao, Y. Zhao, H. Wang, G. Yang, A. Sun and J. Fan, *Energy Environ. Sci.*, 2024, **17**, 4746–4757.

230 S. Wei, C. Wan and Y. Wu, *Green Chem.*, 2023, **25**, 3322–3353.

231 Z. Chen, H. Zheng, J. Zhang, Z. Jiang, C. Bao, C.-H. Yeh and N.-C. Lai, *J. Colloid Interface Sci.*, 2024, **670**, 103–113.

232 S. Zhu, T. Wu, M. Liao, J. Meng, Y. Xie and C. Lu, *Chem. Eng. J.*, 2024, **484**, 149693.

233 F. Zhang, X. Liu, Y. Chen, M. Tian, T. Yang, J. Zhang and S. Gao, *Chin. Chem. Lett.*, 2023, **34**, 108142.

234 X. Zhang, S. Feng, J. Yu, R. Shi, Z. Ma, Z. Yang and L. Yang, *Energy Fuels*, 2022, **36**, 13159–13167.

235 S. S. A. Shah, T. Najam, M. S. Bashir, L. Peng, M. A. Nazir and M. S. Javed, *Energy Storage Mater.*, 2022, **45**, 301–322.

236 W. Shao, R. Yan, M. Zhou, L. Ma, C. Roth, T. Ma, S. Cao, C. Cheng, B. Yin and S. Li, *Electrochem. Energy Rev.*, 2023, **6**, 11.

237 Y. Wang, T. Yang, X. Fan, Z. Bao, A. Tayal, H. Tan, M. Shi, Z. Liang, W. Zhang and H. Lin, *Angew. Chem., Int. Ed.*, 2024, **63**, e202313034.

238 Q. Wang, K. Ye, L. Xu, W. Hu, Y. Lei, Y. Zhang, Y. Chen, K. Zhou, J. Jiang and J. M. Basset, *Chem. Commun.*, 2019, **55**, 14801–14804.

239 X. Bi, Y. Jiang, R. Chen, Y. Du, Y. Zheng, R. Yang, R. Wang, J. Wang, X. Wang and Z. Chen, *Adv. Energy Mater.*, 2024, **14**, 2302388.

240 S. S. Shinde, J. Y. Jung, N. K. Wagh, C. H. Lee, D.-H. Kim, S.-H. Kim, S. U. Lee and J.-H. Lee, *Nat. Energy*, 2021, **6**, 592–604.

241 F. Santos, A. Urbina, J. Abad, R. López, C. Toledo and A. J. Fernández Romero, *Chemosphere*, 2020, **250**, 126273.

242 M. B. Poudel, M. P. Balanay, P. C. Lohani, K. Sekar and D. J. Yoo, *Adv. Energy Mater.*, 2024, **14**, 2400347.

243 Y.-C. Ting, C.-C. Cheng, S.-H. Lin, T.-Y. Lin, P.-W. Chen, F.-Y. Yen, S.-I. Chang, C.-H. Lee, H.-Y. T. Chen and S.-Y. Lu, *Energy Storage Mater.*, 2024, **67**, 103286.

244 Y. Tan, Y. Wang, A. Li, X. Jiang, Y. Zhang and C. Cheng, *J. Energy Chem.*, 2024, **96**, 568–577.

245 J. Gao, D. Pan, K. Chen, Y. Liu, J. Chen and Z. Wen, *Adv. Energy Mater.*, 2024, **14**, 2400368.

246 R. Li, W. Fan, P. Rao, J. Luo, J. Li, P. Deng, D. Wu, W. Huang, C. Jia, Z. Liu, Z. Miao and X. Tian, *ACS Nano*, 2023, **17**, 18128–18138.